

1       **Occurrence frequency of subcritical Richardson number**  
2       **assessed by global high-resolution radiosonde and ERA5**  
3                               **reanalysis**

4  
5       Jia Shao<sup>1</sup>; Jian Zhang<sup>2\*</sup>; Wuke Wang<sup>3</sup>; Shaodong Zhang<sup>4</sup>; Tao Yu<sup>2</sup>; Wenjun Dong<sup>5,6</sup>

6  
7  
8       <sup>1</sup> College of Informatics, Huazhong Agricultural University, Wuhan 430070, China

9       <sup>2</sup> Hubei Subsurface Multi-scale Imaging Key Laboratory, School of Geophysics and  
10               Geomatics, China University of Geosciences, Wuhan 430074, China

11       <sup>3</sup> School of environmental studies, China University of Geosciences, Wuhan 430074,  
12                               China

13       <sup>4</sup> School of Electronic Information, Wuhan University, Wuhan 430072, China

14       <sup>5</sup> Center for Space and Atmospheric Research (CSAR), Embry-Riddle Aeronautical  
15               University, Daytona Beach, FL, USA

16       <sup>6</sup> Global Atmospheric Technologies and Sciences (GATS), Boulder, CO, USA

17  
18  
19  
20       Correspondence to:

21       Dr. Jian Zhang (Email: [zhangjian@cug.edu.cn](mailto:zhangjian@cug.edu.cn))

29 **Abstract.** Kelvin Helmholtz instability (KHI) is most likely to be the primary source  
30 for clear-air turbulence that is of importance in pollution transfer and diffusion and  
31 aircraft safety. It is indicated by the critical value of the dimensionless Richardson ( $Ri$ )  
32 number, which is predicted to be  $1/4$  from linear stability analysis. However,  $Ri$  is fairly  
33 sensitive to the vertical resolution of the dataset; a higher resolution systematically  
34 leads to a finer structure. The study aims to evaluate the performance of ERA5  
35 reanalysis in determining the spatial-temporal variabilities of subcritical  $Ri$  by  
36 comparing it against a near-global high-resolution radiosonde dataset during years 2017  
37 to 2022 and further highlight global climatology and dynamical environment of  
38 subcritical  $Ri$ . Overall, the occurrence frequency of  $Ri < 1/4$  is inevitably underestimated  
39 by the ERA5 reanalysis over all climate zones at all heights from near-ground up to 30  
40 km, compared to radiosonde, due largely to the severe underestimation in wind shears.  
41 Otherwise, the occurrence frequency of  $Ri < 1$  in ERA5 is climatologically consistent  
42 with that from  $Ri < 1/4$  in radiosondes in the free troposphere, especially over the  
43 midlatitude and subtropics in the Northern/Southern Hemisphere. Therefore, we argue  
44 that threshold value of  $Ri$  could be approximated as 1 rather than  $1/4$  when using ERA5-  
45 based  $Ri$  as proxy for KHI. The occurrence frequency of subcritical  $Ri$  revealed by both  
46 datasets exhibits significant seasonal cycles over all climate zones. In addition, it is  
47 positively correlated with the standard derivation of orography at low-levels and is  
48 exceptionally strong over the Niño 3 region at heights of 6–13 km. Furthermore, high  
49 occurrence of subcritical  $Ri$  would likely be accompanied by strong wind speeds and  
50 intensive orographic or non-orographic gravity waves.

51

52 **Key words:** High-resolution radiosonde; ERA5 reanalysis; Wind shears; Richardson  
53 number; Gravity waves

54

55

56

## 57 **Introduction**

58 Kelvin Helmholtz instability (KHI) is a common phenomenon in the atmospheric  
59 boundary layer and the free atmosphere (Muschinski and Wode, 1998), and its  
60 wavelengths and depths span a wide range of scales throughout the atmosphere, varying  
61 from few meters or less to 10s of km (Fritts et al., 2011). It contributes to vertical mixing  
62 of heat, momentum, and constituents, and it acts to limit the maximum shears, just to  
63 name a few (Fritts et al., 2011). KHI along with gravity wave (GW) breaking are the  
64 most recognized instabilities in stably stratified flows (Fritts and Rastogi, 1985). KHI  
65 arises preferentially from micro- and mesoscale wind shear intensification, with  
66 maximal occurrence frequency near synoptic scale upper-level frontal zones near jet  
67 streams, with mountain waves, and above the tops of severe thunderstorms (North et  
68 al., 2014). Large wind shear is commonly associated with regions where stability  
69 changes rapidly (e.g., near the top of the boundary layer) and the large wind gradient in  
70 jet stream (Grasmick and Geerts, 2020). In a changing climate, wind shear in the North  
71 Atlantic upper-level jet stream could be increased (Lee et al., 2019), which may  
72 increase clear-air turbulence at cruise altitudes. In turn, KHI can reduce wind shears  
73 and alter tracer gradients where turbulence and mixing are most intense (Fritts et al.,  
74 2022).

75 KHI influences depend on the spatial scales at which they lead to turbulence (Fritts  
76 et al., 2022). Turbulence is by far the most common cause of serious injuries to aircraft  
77 (Williams and Joshi, 2013). Convective instability, shear instability, KHI, and GW  
78 breaking are known to be the major sources for turbulence (Sharman et al., 2012; Ko et  
79 al., 2019; 2022; Lazarus et al., 2021). KHI requires a sufficiently large Reynolds  
80 number and a Richardson ( $Ri$ ) number sufficiently below  $1/4$  to enable KHI formation  
81 and subsequent secondary instability leading to turbulence (Fritts et al., 2022).  $Ri$  is not  
82 a good guide to instability character in general, and  $Ri > 1/4$  does not assure flow stability  
83 for superpositions of mean and GW motions. Despite these caveats,  $Ri < 1/4$  does  
84 provide a reasonable guide to expected local KHI structure in cases where clear KH

85 billows arise, according to the simulation in the mesosphere and lower thermosphere  
86 region (Fritts et al., 2014). Values of  $Ri$  close to zero favor strong instability, deep  
87 billows, and relatively intense turbulence, whereas values of  $Ri$  closer to 1/4 favor weak  
88 instability, shallow billows (Fritts et al., 2011). The Richardson number criterion can  
89 be applied as a turbulence diagnostic in numerical model output (e.g. Sharman and  
90 Pearson, 2017), and it has been used as such in climatological studies on the occurrence  
91 of clear air turbulence (Jaeger and Sprenger, 2007). Kunkel et al. (2019) includes a brief  
92 discussion on the capability of ECMWF models based on case studies to resolve  
93 subcritical Richardson numbers, and argues that the threshold value of  $Ri$  ( $Rit$ ) taken as  
94 1 might be a good proxy for observed KHI. A very recent study by Lee et al. (2023)  
95 also sets  $Rit$  from 0–1 in their climatology on the upper troposphere and lower  
96 stratosphere turbulence diagnostics. Moreover, Zhang et al. (2022) shows that over half  
97 of turbulence exists below  $Ri < 1$  when the environment is beneficial for the development  
98 of turbulence.

99 Turbulent mixing is of crucial importance to mass, energy, momentum transfer, the  
100 dispersion of pollutants, and stratosphere-troposphere exchange. In numerical models,  
101 turbulent dissipation rate, turbulent diffusivity and other parameters representing  
102 turbulent mixing efficiency are the most basic parameters, which need to be accurately  
103 parameterized to evaluate the impact of turbulence effect on matter and energy  
104 distribution (Gavrilov et al., 2005). However, due to the intermittent nature of  
105 turbulence it is generally not resolved in (global) numerical weather prediction models,  
106 even at nowadays common/states of the art horizontal resolutions of the order of tens  
107 of kilometers (Sandu et al., 2019), and it presents a challenge both in observation and  
108 numerical modeling (Sharman et al., 2012; Homeyer et al., 2014; Plougonven and  
109 Zhang, 2014). For this reason, the indices of turbulence, such as large wind shear, small  
110  $Ri$  and the negative squared Brunt-väisälä frequency, could be a great tool to  
111 characterize turbulence (Jaeger et al., 2007).

112 The Richardson number is estimated by the finite differences across thin layers and  
113 is quite sensitive to the vertical resolution of measurements (Haack et al., 2014). Thus,  
114 a proper estimation of  $Ri$  requires a high-resolution measurement of temperature and

115 wind speed. The near-global distributed radiosonde site offers a unique opportunity to  
116 investigate the climatology of subcritical  $Ri$  occurrence frequency. The overview of  
117 subcritical  $Ri$  occurrence by using a near-global high-resolution (10-m) radiosonde data  
118 was presented in Zhang et al. (2022), and a close association between subcritical  $Ri$   
119 occurrence frequency and turbulence fraction has been found. However, the global  
120 climatology characteristic of subcritical  $Ri$  remains most unclear, especially over  
121 oceans where the radiosonde network has a poor coverage.

122 By comparison, ERA5 global reanalysis can provide a seamless coverage of  
123 temperature and wind, and it is the latest generation of the European Centre for  
124 Medium-Range Weather Forecasts (ECMWF) atmospheric reanalysis and is based on  
125 the state-of-the-art Integrated Forecasting System (IFS) Cy41r2 (Hersbach et al., 2020;  
126 Gu et al., 2023). Its predecessor, ERA-Interim, was found in particular wind shear a  
127 factor of 2–3 lower simulated based on high-resolution radiosondes (Houchi et al.,  
128 2010). Moreover, results show that whatever the location and the geophysical  
129 conditions considered, biases between ERA-Interim and balloon wind measurements  
130 increase as a function of altitude (Duruiseau et al., 2017). Recent studies have  
131 suggested that the structure and variability of the trade winds in the lower troposphere  
132 are reasonably reproduced in the ERA5 reanalysis based on the EUREC4A field  
133 campaign (Savazzi et al., 2022). However, the similar comparison between ERA5 and  
134 high-resolution radiosonde across a near-global area has largely been undetermined.  
135 The proper estimation of wind shear and Brunt-Väisälä frequency is essential for the  
136 determination of  $Ri$ .

137 Thus, our objectives are to: (1) Evaluate the performance of ERA5 at different  
138 heights and climate zones in estimating wind shear and small Richardson number  
139 occurrence frequencies, in comparison with a large high-resolution radiosonde dataset  
140 spanning the years from 2017 to 2022. (2) Based on the validation and comparison  
141 results, we pose a question: how to use ERA5 for subcritical  $Ri$  estimation? (3) The  
142 global climatology of subcritical  $Ri$  occurrence based on versatile measurements and  
143 model products. (4) The dynamic environment (GWs and mean flow) of subcritical  $Ri$ .  
144 These works would be valuable for the understanding of the global distribution of

145 subcritical  $Ri$ , and furthermore, turbulence fraction. To this end, this analysis is  
146 organized as follows. Section 2 shows the data and methods used. Section 3 represents  
147 the climatological variation of subcritical  $Ri$  and its comparison with radiosonde.  
148 Section 4 ends with a summary.

149

## 150 **2 Data and methods**

### 151 **2.1 High-resolution radiosonde dataset**

152 As described in Guo et al. (2021) and Zhang et al. (2022), a high vertical resolution  
153 radiosonde (HVRRS) dataset gained from several organizations was adopted, spanning  
154 January 2017 to October 2022, in a total of 5.8 years. The organizations include the  
155 China Meteorological Administration (CMA), the U.S National Oceanic and  
156 Atmospheric Administration (NOAA), the Global Climate Observing System (GCOS)  
157 Reference Upper-Air Network (GRUAN), the Centre for Environmental Data Analysis  
158 of the United Kingdom (CEDA), University of Wyoming, Deutscher Wetterdienst, and  
159 ECMWF. In total, around 0.95 million radiosonde profiles from 434 radiosonde stations  
160 released at regular synoptic times of 0000 UTC and 1200 UTC were collected to  
161 determine the value of  $Ri$ . These profiles were sampled at 0.5 Hz or 1 Hz, corresponding  
162 to a vertical resolution of approximately 10 m or 5 m. Thus, all the profiles were evenly  
163 interpreted to 10 m resolution in vertical by applying a cubic spline interpolation. In  
164 addition, the sounding with the burst height lower than 10 km above ground level (a.g.l.)  
165 was directly discarded for further study. Meteorological variables, including  
166 temperature and wind speed, were prepared for the  $Ri$  estimation.

167 One of the shortages of radiosonde measurements is its inadequate concentration  
168 over the polar and ocean regions (Xia et al., 2021). The geographical distribution of  
169 total profile number of each radiosonde station is demonstrated in Figure S1 in the  
170 supporting information. The released radiosoundings over Europe, the United States,  
171 and Australia have good geographical coverage and time duration. Over some islands

172 of oceans (e.g., the Pacific Ocean) there are dozens of stations that can provide high-  
173 resolution measurement. Over the polar regions, there are around thirty stations.

## 174 **2.2 ERA5 reanalysis and the collocation procedure**

175 ERA5 is the latest version of ECMWF meteorological reanalysis, benefiting from  
176 a decade of developments in model physics, core dynamics, and data assimilation  
177 (Hersbach et al., 2020). The wind and temperature fields are modelled by the ERA5  
178 reanalysis on a spatial resolution of  $0.25^\circ$  latitude/longitude and a temporal resolution  
179 of 1 hour. The reanalysis has 137 model levels, giving a vertical resolution of  
180 approximately 300 m in the middle and upper troposphere. The vertical resolution of  
181 ERA5 is illustrated in Figure S2. Compared to ERA5, the HVRRS does not provide  
182 global seamless observations. Thus, the collocation procedure between reanalysis and  
183 HVRRS goes as follows: (1) the matched grid of ERA5 reanalysis is the nearest  
184 neighbor of radiosonde station; (2) the regular synoptic start time of radiosonde and  
185 reanalysis needs to keep exact the same; (3) the model level of reanalysis that follows  
186 a hybrid sigma-pressure coordinate, is converted into geopotential height to match with  
187 HVRRS.

188 In addition, the standard deviations of orography (SDOR) and the gravity wave  
189 dissipation due to the effects of stress associated with unresolved valleys, hills and  
190 mountains in ERA5 reanalysis are extracted.

191 The relative error between HVRRS-based and ERA5-based quantities is estimated  
192 by the ratio of deviations between HVRRS and ERA5 derived quantities to the HVRRS  
193 one.

## 194 **2.3 The occurrence frequency of subcritical $Ri$ and its uncertainty**

195 Based on a linear theory, the threshold  $Ri$  ( $Ri_t$ ) defines the threshold where the air  
196 flow changes from stability to turbulence, and it is usually suggested to be  $1/4$  (Haack  
197 et al., 2014).  $Ri$  is formulated as:

$$198 \quad Ri = \bar{N}^2 / \bar{S}^2 \quad (1)$$

199 where  $N$  is the Brunt-Väisälä frequency ( $\sqrt{\frac{g}{\theta} \frac{d\theta}{dz}}$ ),  $S$  is the vertical wind shear  
200 ( $\sqrt{\left(\frac{dU}{dz}\right)^2 + \left(\frac{dV}{dz}\right)^2}$ ), and the overbar denotes a moving average in a 200-m bin to  
201 eliminate the influence of measurement noises and small-scale fluctuations, such as  
202 turbulence and small-scale waves. For a vertical resolution of 10-m, the averaged  
203 parameter at altitude  $i$  can be represented as  $\bar{A}(i) = \frac{1}{n} \sum_{j=i-10}^{i+10} A(j)$ , where  $A$  denotes  
204 wind shear or Brunt-Väisälä frequency and  $n$  is the number of vertical bin. In addition,  
205 horizontal winds measured under radiosonde at the scale of a few tens of meters are  
206 affected by the chaotic movements of the gondola due to the pendulum and to the  
207 balloon's own movements (Ingleby et al., 2022). However, it is hard to quantify the  
208 movement in present study.

209 The Richardson number calculated from Eq.(1) depends on the vertical resolution  
210 of the underlying data, as well as on the averaging interval. Ultimately, this influences  
211 the estimated occurrence frequency for subcritical Richardson numbers as a proxy for  
212 KHI. We resample the HVRRS data to 50 m and 100 m, and range the length scale of  
213 overbar from 100 m to 500 m, to diagnose the uncertainties raised by the length scale  
214 of segments and the vertical resolution of dataset. As indicated in Figure 1, under the  
215 same length scale of overbar, a sparser vertical grid inevitably leads to a lower  
216 occurrence frequency of subcritical  $Ri$ . For instance, as the length scale set to 100 m,  
217 the occurrence frequency of  $Ri < 1/4$  at 0–2 km above sea level (a.s.l.) decreases from  
218 22% when vertical resolution is equal to 10 m to 16% for a vertical resolution of 50 m.  
219 Moreover, a longer length-scale of segment generally yields a smaller occurrence  
220 frequency. For example, as the vertical resolution of radiosonde is equal to 10 m, the  
221 occurrence frequency at 10–15 km decreases from 9% when the length scale of segment  
222 equals 100 m to 1% when it equals 500 m. It is interesting to note that the occurrence  
223 frequency under a vertical resolution of 50 m and a segment interval of 100 m is a bit  
224 larger than that under a vertical resolution of 10 m and a segment of 200 m, possibly  
225 implying the fact that a shorter segment interval could be expected for a sparser vertical  
226 resolution.



## 227 2.4 Gravity wave energy

228 The GW energy is extracted based on the broad spectral method, according to Wang  
229 and Geller (2003). In this method, the magnitude of measured zonal wind ( $u$ ),  
230 meridional wind ( $v$ ), and temperature ( $T$ ) consisting of background states ( $u_0$ ,  $v_0$  and  
231  $T_0$ ) that are determined by applying a second-order polynomial fit (Chen et al., 2018;  
232 Zhang et al., 2022) and perturbations. Therefore, total perturbations are derived as:

$$233 \quad (u', v', T') = (u, v, T) - (u_0, v_0, T_0) \quad (2)$$

234 The perturbations could include measurement noises, KH waves, GWs, and  
235 planetary waves. Only the perturbations with vertical wavelengths of 0.3–6.9 km are  
236 considered as GWs (Wang and Geller, 2003). The mean vertical wavelength of GWs is  
237 about 2 km (Wang et al., 2005), and therefore, the lowermost threshold of 0.3 km could  
238 have little influence on the GW energy. However, the retrieval of the largest wavelength  
239 is not well determined, which is acknowledged as the radiosonde’s “observational filter”  
240 (Alexander, 1998). By applying this band-pass filter, the average gravity-wave kinetic  
241 energy per unit mass (energy density) and the average potential energy density can be  
242 expressed as:

$$243 \quad E_k = \frac{1}{2} [\overline{u'^2} + \overline{v'^2}] \quad (3)$$

$$244 \quad E_p = \frac{1}{2} \frac{g^2 \overline{\hat{T}'^2}}{N^2} \quad (4)$$

245 where  $g$  is the gravitational constant,  $\hat{T}' = T'/\bar{T}$  the normalized perturbation  
246 temperature, and the overbar indicates an averaging over the tropospheric segment,  
247 which is chosen as 2–8.9 km for all regions, except the polar region, and it is selected  
248 as 2–7.4 km for the polar region (Wang and Geller, 2003). Eventually, the total GW  
249 energy  $E_t$  is the sum of  $E_k$  and  $E_p$ .

## 250 3 Results and Discussions

### 251 3.1 Comparisons of wind shear between HRRRS and ERA5 reanalysis

252 The variations in vertical shear of horizontal wind speed and the squared Brunt-

253 väisälä frequency entirely determine the  $Ri$  magnitude. Figure 2 provides an overview  
254 of the spatial distribution of wind shear at heights of 0–2 km a.g.l. and 10–15 km a.g.l.  
255 obtained from the HVRRS and ERA5 reanalysis. HVRRS-based wind shear is taken  
256 from Eq.(1), with a vertical resolution of 10-m. The shear at heights of 0–2 km a.g.l.  
257 estimated by ERA5 reanalysis demonstrates a strong spatial variation, and it is largely  
258 dependent on underlying terrains and latitudes (Fig.2a). For example, large values can  
259 most likely be observed along the coastline, which could be attributed to the prevailing  
260 sea-breeze circulation. As compared to the HVRRS, these shears are slightly  
261 underestimated by 3.30 m/s/km, based on all sounding measurements (Fig.2b).  
262 Nevertheless, a close association between averaged ERA5-reterived shears and  
263 HVRRS-determined shears can be noticed in terms of geospatial distribution, with a  
264 correlation coefficient of 0.48 (Fig. 2b).

265 It is noteworthy that shear in the ERA5 reanalysis at heights of 10–15 km a.g.l. is  
266 significantly underestimated compared to the HVRRS, especially at middle latitudes,  
267 with a mean absolute error for all stations of about 8 m/s/km (Table 1). The  
268 underestimation could partly be due to the coarse vertical resolution (around 300-m) in  
269 the ERA5 reanalysis in this height interval. However, the spatial distribution of the  
270 ERA5 shear still exhibits a significant positive correlation with the HVRRS shear, with  
271 a correlation coefficient of 0.44 (Fig.2d).

272 Following Houchi et al. (2010), the monthly shears over seven typical climate  
273 zones are separately investigated (Fig. 3), which are defined as follows: polar ( $70^{\circ}$ –  
274  $90^{\circ}$ ), mid latitudes ( $40^{\circ}$ – $70^{\circ}$ ), subtropics ( $20^{\circ}$ – $40^{\circ}$ ), and tropics ( $20^{\circ}$  S– $20^{\circ}$  N). Over the  
275 polar region in the Northern/Southern Hemisphere, HVRRS-based shears are  
276 exceptionally strong in the lower stratosphere compared to those in the troposphere  
277 (Fig.3a, g), which could be attributed to the stratospheric polar jet. However, the similar  
278 altitude variation can hardly be found in ERA5-based shears that are dramatically  
279 underestimated by around 12 m/s/km in the lower stratosphere (Fig.3h, n, also seen in  
280 Table 1). The results in midlatitudes reach a similar conclusion (Fig.3b, f, i, m). Over  
281 subtropical regions, HVRRS-based shears are consistent strong at heights of 16–21 km  
282 a.g.l., just above the subtropical jet stream (Fig.3c, e). However, in the ERA5 reanalysis,

283 the region with consistently strong shears can be noticed at approximately 16 km a.g.l.  
284 (Fig.3j, l), which is about 3 km lower than that in the HVRRS. One possible reason  
285 might be that the model fails to resolve the further increasing shear in the lower  
286 stratosphere. In the tropics, the signature of quasi-biennial oscillation (QBO) can be  
287 identified in the lower stratosphere (Fig.3d, k).

288 The comparison between HVRRS-based and ERA5-based shears at three typical  
289 regimes is tabulated in Table 1. These metrics highlight that ERA5-based shears are  
290 underestimated by approximately 3.92 m/s/km, 7.65 m/s/km, 11.99 m/s/km at heights  
291 of 0–2 km, 10–15 km, and 20–25 km a.g.l., respectively, which are roughly consistent  
292 with Houchi et al. (2010).

293 By comparison, the ERA5-acquired  $N^2$  averaged over four height intervals (e.g.,  
294 0–5, 5–10, 10–15, 15–20 km a.g.l.) is reliably estimated at all heights, with a relative  
295 error of around 11%, as illustrated in Figure S3. This finding indicates that the ERA5  
296 reanalysis can properly present the static stability of the background atmosphere, but it  
297 is not properly coincident with radiosonde in terms of the small-scale variability of  
298 dynamical structures. Due to a lack of global measurement of the fine-structure of the  
299 upper-air wind, however, the accuracy of ERA5-resolved shears is hard to be globally  
300 validated.

### 301 **3.2 Occurrence frequency of $Ri < 1/4$ in HVRRS and ERA5 reanalysis**

302 As a prominent example, the monthly occurrence frequency of  $Ri < 1/4$  over the  
303 Corpus Christi station ( $27.77^\circ$  N,  $-97.5^\circ$  W) during years from January 2017 to  
304 October 2022 is illustrated in Figure 4. As a result, the monthly occurrence rate of  
305  $Ri < 1/4$  in the low troposphere determined from HVRRS is lower than the ERA5-based  
306 one, with mean values of around 10.6% and 16.9%, respectively. In the lowermost 2  
307 km, the vertical resolution of ERA5 reanalysis is less than 200 m, and it is less than the  
308 moving segment interval in Eq.(1). The high occurrence frequency in the low  
309 troposphere could be likely related to the negative or small  $N^2$ . Especially during the  
310 daytime, the planetary boundary layer (PBL) is well mixed due to strong turbulence

311 induced by uprising thermals (Song et al., 2018). In addition, an obvious seasonal cycle  
312 of occurrence frequencies is revealed by HVRRS in the middle and upper troposphere  
313 and has a maximum in winter (December–January–February) and spring (March–  
314 April–May) seasons, which is consistent with the finding in Zhang et al. (2019). In the  
315 vicinity of jet streams, the occurrence frequency of  $Ri < 1/4$  is generally enhanced by  
316 large wind shears. However, the ERA5 reanalysis does not provide such a seasonal  
317 cycle pattern, and the occurrence frequency of  $Ri < 1/4$  is significantly underestimated  
318 by around 8% (Fig.4b), which could be attributed to the underestimation in wind shears.  
319 In the lower stratosphere, both the HVRRS and ERA5 reanalysis provide a low  
320 estimation of occurrence frequencies, with a value of around 1%.

321 Furthermore, on a large spatial scale the occurrence frequency of  $Ri < 1/4$  retrieved  
322 by ERA5 reanalysis is remarkably underestimated in the free atmosphere, as compared  
323 to the HVRRS. The annual variation of the occurrence frequency of  $Ri < 1/4$  over seven  
324 climate zones at 10–15 km a.g.l. indicated by HVRRS and ERA5 reanalysis is further  
325 demonstrated in Figure 5. It is clearly seen that the occurrence frequency of  $Ri < 1/4$   
326 provided by ERA5 reanalysis is underestimated in all months, over all climate zones,  
327 possibly implying that, in the free atmosphere, the threshold value of  $1/4$  in Eq.(1) is  
328 too small for the ERA5 reanalysis to capture the occurrence of KHI.

329 However, the ERA5 reanalysis data is non-uniformly sampled in altitude. Its  
330 vertical resolution drops from about 100-m in the boundary layer to about 500-m in the  
331 lower stratosphere. In contrast, radiosondes have a vertical resolution of 10-m at all  
332 heights. Therefore, we selected four typical heights and vertically interpolated the  
333 radiosonde to the same height resolution as ERA5 for comparison. The four height  
334 intervals are 0.8–1.3 km, 2.2–3.2 km, 6–15 km and 20–21 km a.g.l., as shown in Table  
335 2. In these height intervals, the vertical resolution of ERA5 is about 100-m, 200-m, 300-  
336 m and 400-m respectively. Even at the same vertical resolution, ERA5 still seriously  
337 underestimates the value of  $OF(Ri < 1/4)$  at all heights and all climate zones. These  
338 results indicate that the greatest difficulty in evaluating subcritical  $Ri$  with ERA5 is that  
339 its simulation of wind shears might be seriously underestimated compared with  
340 radiosonde. As illustrated in Table 3, even accounting for the fact that ERA5 has a

341 comparable vertical resolution of radiosonde, wind shears in ERA5 reanalysis are still  
342 underestimated by around 50.3%, 48.7%, 43.6%, and 62.2% at 0.8–1.3 km, 2.2–3.2 km,  
343 6–15 km and 20–21 km a.g.l., respectively. In order to obtain an occurrence frequency  
344 of subcritical  $Ri$  from ERA5 reanalysis that is comparable with radiosonde-based  
345  $OF(Ri < 1/4)$ , the  $Rit$  for ERA5 should be set larger than 1/4. For instance, at 0.8–1.3 km  
346 and 2.2–3.2 km a.g.l., the  $Rit$  equals 1 could be a proper choice for ERA5 reanalysis,  
347 rather than 1/4 (Table 2). More generally,  $0.5 < Rit < 1.5$  could be more suitable for ERA5  
348 reanalysis, compared to  $Rit = 1/4$ .

349 Due to the huge change in the vertical resolution of ERA5, it could be difficult to  
350 interpolate ERA5 into uniform data vertically with a relatively high resolution.  
351 Therefore, the question posed here is, what is the proper threshold value of  $Ri$  in  
352 predicting the occurrence of KHI when using the ERA5 reanalysis, compared to  
353 HVRRS? The occurrence frequency of  $Ri < 1/4$  indicated by the HVRRS, the ERA5-  
354 determined occurrence frequencies produced by  $Ri < 0.25$ ,  $Ri < 0.5$ ,  $Ri < 1$ ,  $Ri < 1.5$ , and  
355  $Ri < 2$  at all heights up to 30 km a.g.l. are demonstrated in Figure 6. It is notable that  
356 over all climate zones and in the free atmosphere, occurrence frequencies of  $Ri < 0.25$   
357 and  $Ri < 0.5$  obtained from the ERA5 reanalysis are underestimated, but the frequencies  
358 of  $Ri < 1.5$  and  $Ri < 2$  are generally overestimated. The occurrence frequency of  $Ri < 1$   
359 gives a close estimation both in magnitude and spatial variation compared to HVRRS  
360 over all climate zones.

361 Furthermore, the correlation coefficients between HVRRS-determined  
362 occurrence frequency and the ERA5-determined frequencies indicated by different  
363 threshold values of  $Ri$  at height levels of 0 to 30 km are illustrated in Figure 7. It is  
364 worth noting that, in the troposphere, the ERA5-based frequencies indicated by  $Ri < 1$ ,  
365  $Ri < 1.5$ , and  $Ri < 2$  are highly positively correlated with those from the HVRRS, with a  
366 correlation coefficient of around 0.6 over all climate zones. In the lower stratosphere,  
367 however, these coefficients rapidly decline to 0.1, which can be explained by the low  
368 occurrence frequency in this height regime.

369 Combined the findings in Figures 6 and 7, in the free troposphere, we can conclude  
370 that the ERA5-determined occurrence frequency of  $Ri < 1$  is closest to the frequency of

371  $Ri < 1/4$  based on the HVRRS. In the free atmosphere, KHI is the dominant source for  
372 clear-air turbulence (CAT) that is a well-known hazard to aviation. Therefore, the global  
373 characterization of KHI occurrence frequency in the free atmosphere obtained from  
374 ERA5 reanalysis could be of importance for understanding the spatial-temporal  
375 variation of CAT. In the following sections, the occurrence frequency of subcritical  $Ri$   
376 (hereinafter  $OF(Ri < Rit)$ ) is based on  $Ri < 1$  in ERA5 reanalysis and  $Ri < 1/4$  in HVRRS,  
377 unless otherwise noted.

378 Finally, it is noteworthy that  $OF(Ri < Rit)$  includes the component of  $Ri < 0$  that  
379 indicates potential for convective instability. However, both ERA5 and HVRRS are  
380 difficult to totally avoid  $Ri < 0$  when calculating  $Ri$ . Therefore, we evaluated the  
381 proportion of  $Ri < 0$  in all  $Ri < Rit$  in the two datasets to evaluate the possible contribution  
382 from convection, as shown in Figure 8. For HVRRS, the proportion of  $OF(Ri < 0)$  drops  
383 sharply from about 40% in the low troposphere to about 18% at 5–15 km a.g.l..  
384 Similarly, for ERA5 its proportion drops from about 40% in the lowermost part of the  
385 atmosphere to about 2% at 5–16 km a.g.l.. These findings indicate that, in the free  
386 atmosphere,  $OF(Ri < Rit)$  is mainly composed of  $OF(0 < Ri < Rit)$ , which implies that local  
387 instabilities constitute most of the dynamic instability.

### 388 **3.3 The $OF(Ri < Rit)$ climatology**

389 For a first hint the global distributions of  $OF(Ri < Rit)$  provided by the ERA5  
390 reanalysis at 0–2 km, 5–10 km, 10–15 km, and 15–20 km a.g.l. are displayed in Figure  
391 9.  $OF(Ri < Rit)$  in the low troposphere is considerably spatially heterogeneous. Over  
392 subtropical oceans in the Northern/Southern Hemisphere, the intense  $OF(Ri < Rit)$  can  
393 be noticed and has a magnitude of around 50% (Fig.9a). In addition, over the Sahara  
394 Desert the  $OF(Ri < Rit)$  reaches as high as 65%. Interestingly, the spatial variation in  
395  $OF(Ri < Rit)$  ensembled by years 2017 to 2022 keeps high consistency with that of  
396 planetary boundary layer height (PBLH) over oceans, such as the Pacific Ocean near  
397 Japan and the Atlantic Ocean near U.S., as shown in Figure S4. However, at 0–2 km  
398 a.g.l., the spatial variation of  $OF(0 < Ri < Rit)$  exhibits a large difference with that of

399  $OF(Ri < Rit)$  in terms of magnitude, as shown in Figure S5. It is around 40% (20%) lower  
400 than that of  $OF(Ri < Rit)$  over subtropical oceans (Australia and North Africa). At heights  
401 of 5–10 km a.g.l., intensive  $OF(Ri < Rit)$  can be viewed over the subtropic regions and  
402 has a value of around 10% (Fig.9b), which is likely attributed to upper tropospheric jets.  
403 In the upper troposphere over the tropical oceans,  $OF(Ri < Rit)$  is as high as 30% (Fig.9c),  
404 possibly as a result of the maximal heating effect by mesoscale convective systems (e.g.,  
405 Houze 1982). In the lower stratosphere,  $OF(Ri < Rit)$  sharply decreases to around 0.1%  
406 (Fig.9d).

407 In comparison, the spatial-temporal variability of  $OF(Ri < Rit)$  indicated by HVRRS  
408 keeps highly consistency with that of ERA5 reanalysis over all climate zones and in the  
409 free troposphere, except in the stratosphere of polar region (Figure 10). Seasonal cycles  
410 can be detected by both the HVRRS and ERA5 reanalysis over all climate zones,  
411 especially over subtropics and midlatitude regions. However, the ERA5-based  
412  $OF(Ri < Rit)$  can only reflect the large scale structure of the cycles, and it is hard to  
413 quantify the detailed variation like the HVRRS does.

414 Furthermore, the seasonal variation of  $OF(Ri < Rit)$  with  $Rit=1/4$  for HVRRS and  
415  $Rit=1$  for ERA5 for all climate zones is further analyzed in Figure 11. In the  
416 midlatitudes and subtropics, the  $OF(Ri < Rit)$  exhibits maximum values in the low  
417 troposphere, as well as a local minimum in the middle troposphere and a local  
418 maximum at altitudes around 9 km. In the stratosphere the occurrence frequencies  
419 decrease to values of the order of 1% (Fig.11b,c,e,f). Over tropic regions, a primary  
420 peak can be clearly noticed at around 13 km, with a maximum of 12% for the HVRRS  
421 and 20% for the ERA5 reanalysis (Fig.11d, k). The seasonality over the tropical region  
422 could be related to some large scale flow features like the Summer Asian Monsoon and  
423 the tropical easterly jet (Roja Raman et al., 2009; Sunilkumar et al., 2015; Kaluza et al.,  
424 2021). Over polar regions, the tropospheric  $OF(Ri < Rit)$  is significantly lower than that  
425 over other climate zones, with values ranging from around 4% at heights of 2–8 km to  
426 1% in the lower stratosphere (Fig.11a,g).

427 In Table 4, the mean  $OF(Ri < Rit)$  magnitudes over seven climate zones and at three  
428 typical altitude regimes are listed. At 0–2 km a.g.l., the ERA5-based  $OF(Ri < Rit)$  is

429 about 24% larger than that of the HVRRS-based one. At 10–15 km a.g.l., the ERA5-  
430 based  $OF(Ri < Rit)$  is reasonably well estimated, except that it is overestimated by  
431 around 5.92% over the tropics region. In addition, ERA5 underestimates  $OF(Ri < Rit)$   
432 by around 0.5% in the lower stratosphere.

433 According to Fig.9a, it seems that low-level continental  $OF(Ri < Rit)$  is dependent  
434 on underlying terrains. We investigate the association of low-level HVRRS-determined  
435  $OF(Ri < Rit)$  with the standard deviation of orography (SDOR). At heights of 1–2 km  
436 a.g.l., the underlying terrain with a large SDOR generally corresponds to a high  
437  $OF(Ri < Rit)$ , with a correlation coefficient between  $OF(Ri < Rit)$  and SDOR of 0.24.  
438 Then, the coefficient decreases to 0.15 at 3–4 km a.g.l. (Fig.12b), and eventually, it  
439 equals 0.14 at 5–6 km a.g.l. (Fig.12c). These findings indicate that, complex terrain  
440 may locally enhance  $OF(Ri < Rit)$ .

441 Moreover, it is quite evident from Fig.9b and Fig.S5 that both  $OF(Ri < Rit)$  and  
442  $OF(0 < Ri < Rit)$  are largely enhanced over the tropical ocean associated with the El Niño  
443 Southern Oscillation (ENSO). The most of the enhanced  $OF(Ri < Rit)$  can be identified  
444 over the Niño 3 region ( $5^{\circ}\text{N}$ – $5^{\circ}\text{S}$ ,  $150^{\circ}\text{W}$ – $90^{\circ}\text{W}$ ), and the time-height cross section  
445 of  $OF(Ri < Rit)$  during years of 2000 to 2022 is illustrated in Figure 13. The  $OF(Ri < Rit)$   
446 at height region of 6–13 km are evidently large, with values of around 35%, which is  
447 about 15% larger than the climatological mean value (Fig.10k). More specifically,  
448  $OF(Ri < Rit)$  during time periods of La Niña events is obviously stronger than that during  
449 the El Niño periods. The identification of ENSO events is based on Ren et al. (2018),  
450 Li et al. (2022), and Lv et al. (2022). It is also worth recalling here that the wind shear  
451 does not exhibit such an anomaly over the Niño 3 region (Fig.2c), implying that the  
452  $OF(Ri < Rit)$  anomaly could likely be attributed to the ENSO-related tropical convective  
453 heating in the upper troposphere, leading to a low Brunt-Väisälä frequency.

#### 454 **3.4 The dynamical environment of $OF(Ri < Rit)$ in the free troposphere**

455 In the free troposphere the percentage of  $OF(Ri < 0)$  relative to  $OF(Ri < Rit)$  is  
456 generally less than 20% (Fig. 8), KHI is preferentially generated from strong wind shear,



457 which may be closely associated with mean flows and wave activities.

458 The propagation of GW could raise strong wind shear, and therefore generate KHI.  
459 Thereby, we investigate the joint distribution of  $OF(Ri < Rit)$  with tropospheric GW total  
460 energy and wind shear (Figure 14). The latitudinal variation of GW total energy exhibits  
461 a double-peak structure, with two peaks at around  $30^\circ$  in the Northern/Southern  
462 Hemisphere (Fig. 14a). The joint distribution of  $OF(Ri < Rit)$  with GW energy and wind  
463 shear indicates that large  $OF(Ri < Rit)$  (for instance, larger than 10%) generally  
464 corresponds to GW energy larger than 10 J/kg or wind shear exceeds 14 m/s/km (Fig.  
465 14b). Also,  $OF(0 < Ri < Rit)$  exhibits a similar distribution (Figure S6). Overall,  
466  $OF(Ri < Rit)$  obviously increases with GW total energy (Figure S9a), possibly implying  
467 that the propagation of GWs could enhance wind shear and therefore, the burst of KHI.

468 In addition, the interaction between low-level wind and mountain barrier could be  
469 a source of orographic GWs (Zhang et al., 2022). We take orographic GW dissipation  
470 in ERA5 reanalysis, which is the accumulated conversion of kinetic energy in the mean  
471 flow into heat over the whole atmospheric column, as an indicator of the strength of  
472 orographic GWs. It is interesting to note that monthly averaged orographic GW  
473 dissipation and monthly ERA5-determined  $OF(Ri < Rit)$  at heights from ground up to 30  
474 km demonstrates a close association (Figure S7). For instance, in the middle  
475 troposphere, they are positively associated over mountainous areas such as the Rocky  
476 Mountains and the Alps Mountain, with correlation coefficients of around 0.5. These  
477 findings also suggest that during months with strong unresolved orographic gravity  
478 wave activity, which then modify the flow and stability parameters of the resolved flow,  
479 leading to a low Richardson number. Nevertheless, it is hard to quantify the effect of  
480 resolved orographic GWs on  $Ri$  here.

481 At jet heights (10–15 km a.g.l.), a large shear can be easily induced by strong wind  
482 speed. Figure 15 demonstrates the joint distribution of  $OF(Ri < Rit)$  with wind speed and  
483 wind shear. Generally,  $OF(Ri < Rit)$  larger than 10% can be easily found when the wind  
484 shear exceeds 20 m/s/km. In addition,  $OF(0 < Ri < Rit)$  draws a similar conclusion (Figure  
485 S8). In the middle and upper troposphere,  $OF(Ri < Rit)$  almost linearly increases with  
486 wind speed (Figure S9b).

487 In a short conclusion, in the free troposphere, the occurrence of KHI would favor  
488 the dynamical environment with intensive orographic or non-orographic GW activities  
489 and large mean flows.

#### 490 **4 Conclusion and remarks**

491 The occurrence of KHI is potential crucial for many implications, such as aircraft  
492 safety and mass transfer, but it is very hard to be globally understood due to its fine  
493 structure. The subcritical Richardson number is commonly used as an indicator for KHI.  
494 This study uses the ERA5 as the latest reanalysis product from the ECMWF as well as  
495 a comprehensive data set of HVRRS radiosonde soundings to globally characterize the  
496 distribution of low Richardson numbers as a proxy for the occurrence of KHI, for the  
497 years 2017 to 2022.

498 Vertical wind shears are considerably underestimated at almost all heights and over  
499 all climate zones by the ERA5 reanalysis, compared to the HVRRS. It is noteworthy  
500 that vertical wind shear in the ERA5 reanalysis at heights of 10–15 km a.g.l. is  
501 dramatically underestimated by around 7.65 m/s/km, especially at middle latitudes.  
502 However, the spatial distribution of the ERA5 shear exhibits a statistically significant  
503 positive correlation with the HVRRS shear. As a result, the ERA5-determined  
504 occurrence frequency of  $Ri < 1/4$  is significantly underestimated. In addition, it is weak  
505 correlated with HVRRS-determined ones at most heights and over most climate zones.

506 However, the vertical resolution of ERA5 reanalysis sharply decreases with altitude,  
507 which is not comparable with HVRRS. Thus, to match with ERA5 reanalysis at  
508 specified height intervals, the HVRRS was vertically interpolated with resolutions  
509 spanning from 100-m to 400-m. Even at a comparable resolution, vertical wind shear  
510 is underestimated by around 50%, leading to a considerable underestimation in  
511  $OF(Ri < 1/4)$ , compared to radiosondes.

512 Interestingly, the ERA5-determined occurrence frequency of  $Ri < 1$  is generally  
513 consistent with the frequency of  $Ri < 1/4$  obtained from HVRRS, in terms of magnitude  
514 and temporal variation. Rather than  $Ri < 1/4$ , we argue that the threshold value of  $Ri < 1$

515 could be more proper when using ERA5 reanalysis for KHI study, especially in the  
516 middle and upper troposphere over midlatitude and subtropic regions in the  
517 Northern/Southern Hemisphere, where a high consistency between HVRRS and ERA5  
518 has been found in terms of  $OF(Ri < Rit)$  magnitude. In other words, under a similar  
519 occurrence frequency, the identification of vertical segments with  $Ri < 1$  in ERA5 is  
520 equitable with identification of vertical segments with  $Ri < 1/4$  using HVRRS. It is worth  
521 highlighting that HVRRS experiences a 200-m vertical moving average procedure to  
522 inhabit measurement noises and turbulence fluctuations. Without this procedure, the  
523 threshold  $Ri$  for the ERA5 reanalysis would even higher than 1.

524 The climatology of  $OF(Ri < Rit)$  exhibits significant seasonal cycles over all  
525 latitudes. A poleward decrease can be clearly identified in the middle and upper  
526 troposphere. In addition, over mountainous area, complex terrain may locally enhance  
527 low-level  $OF(Ri < Rit)$ . Moreover, it is immediately obvious that the both  $OF(Ri < Rit)$   
528 and  $OF(0 < Ri < Rit)$  in the middle and upper troposphere of the Niño 3 region is largely  
529 enhanced probably by the tropical convective heating.

530 Moreover, both  $OF(Ri < Rit)$  and  $OF(0 < Ri < Rit)$  exhibit close relationship with GW  
531 activities and background mean flow. For instance, large  $OF(Ri < Rit)$  favors intensive  
532 GW activities and strong mean flow. Over complex terrains, the orographic GW  
533 breaking could locally enhance  $OF(Ri < Rit)$ .

534 Those findings are valuable for pointing out the performance of the ERA5  
535 reanalysis in terms of resolving low Richardson numbers as a proxy for KHI, in  
536 comparison with a near-global high-resolution radiosonde measurement. In addition,  
537 the spatial-temporal variability of  $OF(Ri < Rit)$  over different climate zones from near-  
538 ground up to 30 km is quantitatively characterized by ERA5 and HVRRS, which could  
539 provide new insights that increase our understanding of the fine structure of upper air.

540

## 541 **Acknowledgement**

542 The authors would like to acknowledge the National Meteorological Information

543 Centre (NMIC) of CMA, NOAA, Deutscher Wetterdienst (Climate Data Center), U.K  
544 Centre for Environmental Data Analysis (CEDA), GRUAN, ECMWF, and the  
545 University of Wyoming for continuously collecting and generously providing high-  
546 resolution radiosonde data. Last but not least, we would like to thank two anonymous  
547 reviewers for their excellent comments that greatly helped to improve our work.  
548

### 549 **Financial support**

550 This study jointly supported by the National Natural Science Foundation of China under  
551 grants 42205074, 62101203 and 42127805, the Hubei Provincial Natural Science  
552 Foundation of China under Grant 2021CFB459, and the Research Grants of Huazhong  
553 Agricultural University under grants No. 2662021XXQD002 and 2662021JC008.  
554

### 555 **Competing interests**

556 The contact author has declared that neither they nor their co-authors have any  
557 competing interests  
558

### 559 **Data availability**

560 The dataset can be accessed at ECMWF (2022).  
561

### 562 **Author contributions**

563 JZ conceptualized this study. JS carried out the analysis with comments from other co-  
564 authors. JZ wrote the original manuscript. WW, SZ, TY, WD provided useful

565 suggestions for the study. All authors contributed to the improvement of paper.

566

## 567 **References**

568 Alexander, M. J.: Interpretations of observed climatological patterns in stratospheric  
569 gravity wave variance, *J. Geophys. Res. Atmos.*, 103(D8), 8627–8640,  
570 <https://doi.org/10.1029/97JD03325>, 1998.

571 Duruisseau, F., N., Huret, A., Andral, and Camy-Peyret, C.: Assessment of the ERA-  
572 Interim winds using high-altitude stratospheric balloons, *J. Atmos. Sci.*, 74(6),  
573 2065–2080, <https://doi.org/10.1175/JAS-D-16-0137.1>, 2017.

574 ECMWF: ECMWF Reanalysis v5 (ERA5), European Centre for Medium-Range  
575 Weather Forecasts [data set],  
576 <https://www.ecmwf.int/en/forecasts/dataset/ecmwf-reanalysis-v5>, last access:  
577 07 December 2022.

578 Fritts, D. C., K. Wan, J. Werne, T. Lund, and Hecht, J. H.: Modeling the implications of  
579 Kelvin-Helmholtz instability dynamics for airglow observations, *J. Geophys.*  
580 *Res. Atmos.*, 119, 8858–8871, <https://doi.org/10.1002/2014JD021737>, 2014.

581 Fritts, D. C., P. M. Franke, K. Wan, T. Lund, and Werne, J.: Computation of clear-air  
582 radar backscatter from numerical simulations of turbulence: 2. Backscatter  
583 moments throughout the lifecycle of a Kelvin Helmholtz instability, *J. Geophys.*  
584 *Res.*, 116, D11105, <https://doi.org/10.1029/2010JD014618>, 2011.

585 Fritts, D. C., and Rastogi, P. K.: Convective and dynamical instabilities due to gravity  
586 wave motions in the lower and middle atmosphere: Theory and observations.  
587 *Radio Sci.*, 20, 1247–1277, <https://doi.org/10.1029/RS020i006p01247>, 1985.

588 Fritts, D. C., L., Wang, T. S., Lund, S. A., Thorpe, C. B., Kjellstrand, B., Kaifler, and  
589 Kaifler, N.: Multi-Scale Kelvin-Helmholtz instability dynamics observed by  
590 PMC Turbo on 12 July 2018: 2. DNS modeling of KHI dynamics and PMC  
591 responses., *J. Geophys. Res. Atmos.*, 127, e2021JD035834.  
592 <https://doi.org/10.1029/2021JD035834>, 2022.

593 Grasmick, C., and Geerts, B.: Detailed dual-Doppler structure of Kelvin–Helmholtz  
594 waves from an airborne profiling radar over complex terrain. Part I: Dynamic  
595 structure, *J. Atmos. Sci.*, 77(5), 1761–1782., [https://doi.org/10.1175/JAS-D-19-](https://doi.org/10.1175/JAS-D-19-0108.1)  
596 0108.1, 2020.

597 Gavrilov, N. M., Luce, H., Crochet, M., Dalaudier, F., and Fukao, S.: Turbulence  
598 parameter estimations from high-resolution balloon temperature measurements  
599 of the MUTSI-2000 campaign, *Ann. Geophys.*, 23, 2401–2413,  
600 [doi:10.5194/angeo-23-2401-2005](https://doi.org/10.5194/angeo-23-2401-2005), 2005

601 Gu, L., Yin, J., Gentine, P. et al.: Large anomalies in future extreme precipitation  
602 sensitivity driven by atmospheric dynamics, *Nat. Commun.*, 14, 3197,  
603 <https://doi.org/10.1038/s41467-023-39039-7>, 2023

604 Guo, J., Zhang, J., Yang, K., Liao, H., Zhang, S., Huang, K., Lv, Y., Shao, J., Yu, T.,  
605 Tong, B., Li, J., Su, T., Yim, S. H. L., Stoffelen, A., Zhai, P., and Xu, X.:  
606 Investigation of near-global daytime boundary layer height using high-  
607 resolution radiosondes: first results and comparison with ERA5, MERRA-2,  
608 JRA-55, and NCEP-2 reanalyses, *Atmos. Chem. Phys.*, 21, 17079–17097,  
609 <https://doi.org/10.5194/acp-21-17079-2021>, 2021.

610 Haack, A., M. Gerding, and Lübken, F.-J.: Characteristics of stratospheric turbulent  
611 layers measured by LITOS and their relation to the Richardson number, *J.*  
612 *Geophys. Res. Atmos.*, 119, 10605–10618,  
613 <https://doi.org/10.1002/2013JD021008>, 2014.

614 Hersbach, H., Bell, B., Berrisford, P., Hirahara, S., Horányi, A., Muñoz-Sabater, J.,  
615 Nicolas, J., Peubey, C., Radu, R., Schepers, D., Simmons, A., Soci, C., Abdalla,  
616 S., Abellan, X., Balsamo, G., Bechtold, P., Biavati, G., Bidlot, J., Bonavita, M.,  
617 De Chiara, G., Dahlgren, P., Dee, D., Diamantakis, M., Dragani, R., Flemming,  
618 J., Forbes, R., Fuentes, M., Geer, A., Haimberger, L., Healy, S., Hogan, R. J.,  
619 Hólm, E., Janisková, M., Keeley, S., Laloyaux, P., Lopez, P., Lupu, C., Radnoti,  
620 G., de Rosnay, P., Rozum, I., Vamborg, F., Villaume, S., and Thépaut, J.-N.: The  
621 ERA5 global reanalysis, *Q. J. Roy. Meteorol. Soc.*, 146, 1999–2049,  
622 <https://doi.org/10.1002/qj.3803>, 2020.

623 Homeyer, C. R., L. L. Pan, and Barth, M. C.: Transport from convective overshooting  
624 of the extratropical tropopause and the role of large-scale lower stratospheric  
625 stability, *J. Geophys. Res. Atmos.*, 119(5), 2220–2240,  
626 <https://doi.org/10.1002/2013JD020931>, 2014.

627 Houchi, K., Stoffelen, A., Marseille, G. J., and De Kloe, J.: Comparison of wind and  
628 wind shear climatologies derived from high-resolution radiosondes and the  
629 ECMWF model, *J. Geophys. Res.-Atmos.*, 115, D22123,  
630 <https://doi.org/10.1029/2009JD013196>, 2010.

631 Houze, R. A., Jr.: Cloud clusters and large-scale vertical motions in the tropics, *J.*  
632 *Meteor. Soc. Japan*, 60, 396–410, [https://doi.org/10.2151/jmsj1965.60.1\\_396](https://doi.org/10.2151/jmsj1965.60.1_396),  
633 1982.

634 Ingleby, B., Motl, M., Marlton, G., Edwards, D., Sommer, M., von Rohden, C., Vömel,  
635 H., and Jauhiainen, H.: On the quality of RS41 radiosonde descent data, *Atmos.*  
636 *Meas. Tech.*, 15, 165–183, <https://doi.org/10.5194/amt-15-165-2022>, 2022.

637 Lazarus, S. M., Chiappa, J., Besing, H., Splitt, M. E., and Rioussset, J. A.: Distinguishing  
638 characteristics of the tropical cyclone gigantic jet environment, *J. Atmos. Sci.*,  
639 78(9), 2741–2761, <https://doi.org/10.1175/JAS-D-20-0265.1>, 2021.

640 Lee, S. H., Williams, P. D., and Frame, T. H.: Increased shear in the North Atlantic  
641 upper-level jet stream over the past four decades, *Nature*, 572, 639–642,  
642 <https://doi.org/10.1038/s41586-019-1465-z>, 2019.

643 Lee, J. H., Kim, J.-H., Sharman, R. D., Kim, J., and Son, S.-W. Climatology of Clear-  
644 Air Turbulence in upper troposphere and lower stratosphere in the Northern  
645 Hemisphere using ERA5 reanalysis data, *J. Geophys. Res.-Atmos.*, 128,  
646 e2022JD037679, <https://doi.org/10.1029/2022JD037679>, 2023.

647 Li, X., Hu, Z. Z., Tseng, Y. H., Liu, Y., and Liang, P.: A historical perspective of the La  
648 Niña event in 2020/2021, *J. Geophys. Res.-Atmos.*, 127(7), e2021JD035546,  
649 <https://doi.org/10.1029/2021JD035546>, 2022.

650 Lv, A., Fan, L., and Zhang, W.: Impact of ENSO Events on Droughts in China,  
651 *Atmosphere*, 13(11), 1764, <https://doi.org/10.3390/atmos13111764>, 2022.

652 Jaeger, E. B., and Sprenger, M.: A Northern Hemispheric climatology of indices for

653 clear air turbulence in the tropopause region derived from ERA40 reanalysis  
654 data, *J. Geophys. Res.*, 112, D20106, doi:10.1029/2006JD008189, 2007.

655 Kaluza, T., Kunkel, D., and Hoor, P.: On the occurrence of strong vertical wind shear  
656 in the tropopause region: a 10-year ERA5 northern hemispheric study, *Weather  
657 Clim. Dynam.*, 2, 631–651, <https://doi.org/10.5194/wcd-2-631-2021>, 2021.

658 Kunkel, D., Hoor, P., Kaluza, T., Ungermann, J., Kluschat, B., Giez, A., Lachnitt, H.-  
659 C., Kaufmann, M., and Riese, M.: Evidence of small-scale quasi-isentropic  
660 mixing in ridges of extratropical baroclinic waves, *Atmos. Chem. Phys.*, 19,  
661 12607–12630, <https://doi.org/10.5194/acp-19-12607-2019>, 2019.

662 Ko, H. C., H. Y., Chun, R., Wilson, and Geller, M. A.: Characteristics of  
663 atmospheric turbulence retrieved from high vertical-resolution radiosonde  
664 data in the United States, *J. Geophys. Res. Atmos.*,  
665 124, <https://doi.org/10.1029/2019JD030287>, 2019.

666 Ko, H. C. and Chun, H. Y.: Potential sources of atmospheric turbulence estimated using  
667 the Thorpe method and operational radiosonde data in the United States. *Atmos.  
668 Res.*, 265, 105891, <https://doi.org/10.1016/j.atmosres.2021.105891>, 2022.

669 Muschinski, A., and Wode, C.: First in situ evidence for coexisting submeter  
670 temperature and humidity sheets in the lower free troposphere, *J. Atmos. Sci.*,  
671 55(18), 2893–2906, [https://doi.org/10.1175/1520-  
672 0469\(1998\)055<2893:FISEFC>2.0.CO;2](https://doi.org/10.1175/1520-0469(1998)055<2893:FISEFC>2.0.CO;2), 1998.

673 North, G. R., Pyle, J. A., and Zhang, F.: *Encyclopedia of atmospheric sciences*,  
674 Academic Press, Cambridge, Massachusetts, United States, 224 pp., 2014

675 Plougonven, R., and Zhang, F.: Internal gravity waves from atmospheric jets and fronts,  
676 *Rev. Geophys.*, 52, 33–76, <https://doi.org/10.1002/2012RG000419>, 2014.

677 Ren, H. L., B., Lu, J., Wan, B., Tian, and Zhang, P.: Identification standard for ENSO  
678 events and its application to climate monitoring and prediction in China, *J.  
679 Meteorol. Res.*, 32, 923–936, <https://doi.org/10.1007/s13351-018-8078-6>, 2018.

680 Roja Raman, M., Jagannadha Rao, V. V., Venkat Ratnam, M., Rajeevan, M., Rao, S. V.,  
681 Narayana Rao, D., and Prabhakara Rao, N.: Characteristics of the Tropical  
682 Easterly Jet: Long-term trends and their features during active and break



683 monsoon phases, *J. Geophys. Res.-Atmos.*, 114, 1–14,  
684 <https://doi.org/10.1029/2009JD012065>, 2009.

685 Sandu, I., A., A., van Niekerk, T. G., Shepherd, S. B., Vosper, A., Zadra, J., Bacmeister,  
686 et al: Impacts of orography on large-scale atmospheric circulation. *npj Clim*  
687 *Atmos Sci*, 2(1), 1–8, <https://doi.org/10.1038/s41612-019-0065-9>, 2019.

688 Savazzi, A. C. M., Nuijens, L., Sandu, I., George, G., and Bechtold, P.: The  
689 representation of the trade winds in ECMWF forecasts and reanalyses during  
690 EUREC<sup>4</sup>A, *Atmos. Chem. Phys.*, 22, 13049–13066,  
691 <https://doi.org/10.5194/acp-22-13049-2022>, 2022.

692 Sharman, R. D., S. B. Trier, T. P. Lane, and Doyle., J. D.: Sources and dynamics of  
693 turbulence in the upper troposphere and lower stratosphere: A review, *Geophys.*  
694 *Res. Lett.*, 39, L12803, <https://doi.org/10.1029/2012GL051996>, 2012.

695 Sharman, R. D., and Pearson, J. M: Prediction of energy dissipation rates for aviation  
696 turbulence. Part I: Forecasting nonconvective turbulence. *J. Appl. Meteorol.*  
697 *Climatol*, 56(2), 317–337, <https://doi.org/10.1175/JAMC-D-16-0205.1>, 2017.

698 Song, J., Z.-H., Wang, and Wang, C.: The regional impact of urban heat mitigation  
699 strategies on planetary boundary layer dynamics over a semiarid city, *J.*  
700 *Geophys. Res. Atmos.*, 123(12), 6410–6422,  
701 <https://doi.org/10.1029/2018JD028302>, 2018.

702 Sunilkumar, S. V., Muhsin, M., Parameswaran, K., Venkat Ratnam, M., Ramkumar,  
703 G., Rajeev, K., Krishna Murthy, B. V., Sambhu Namboodiri, K. V.,  
704 Subrahmanyam, K. V., Kishore Kumar, K., and Shankar Das, S.: Characteristics  
705 of turbulence in the troposphere and lower stratosphere over the Indian  
706 Peninsula, *J. Atmos. Sol.-Terr. Phys.*, 133, 36–53,  
707 <https://doi.org/10.1016/j.jastp.2015.07.015>, 2015.

708 Wang, L., and Geller, M. A.: Morphology of gravity-wave energy as observed from 4  
709 years (1998–2001) of high vertical resolution U.S. radiosonde data, *J. Geophys.*  
710 *Res. Atmos.*, 108(D16), 4489, <https://doi.org/10.1029/2002JD002786>, 2003.

711 Wang, L., Geller, M. A., and Alexander, M. J.: Spatial and Temporal Variations of  
712 Gravity Wave Parameters, Part I: Intrinsic Frequency, Wavelength, and Vertical

713 Propagation Direction, *J. Atmos. Sci.*, 62, 125–142,  
714 <https://doi.org/10.1175/JAS-3364.1>, 2005

715 Williams, P. D., and Joshi, M. M.: Intensification of winter transatlantic aviation  
716 turbulence in response to climate change. *Nat. Clim. Chang.*, 3(7), 644–648,  
717 <https://doi.org/10.1038/nclimate1866>, 2013.

718 Xia, P., Y., Shan, S., Ye, and Jiang, W.: Identification of Tropopause Height with  
719 Atmospheric Refractivity, *J. Atmos. Sci.*, 78(1), 3–16  
720 <https://doi.org/10.1175/JAS-D-20-0009.1>, 2021.

721 Zhang, J., S. D., Zhang, C. M., Huang, K. M., Huang, Y., Gong, Q., Gan, and Zhang,  
722 Y. H.: Latitudinal and topographical variabilities of free atmospheric turbulence  
723 from high-resolution radiosonde data sets, *J. Geophys. Res. Atmos.*, 124, 4283–  
724 4298. <https://doi.org/10.1029/2018JD029982>, 2019.

725 Zhang, J., J., Guo, H., Xue, S., Zhang, K., Huang, W. Dong, et al.: Tropospheric gravity  
726 waves as observed by the high-resolution China radiosonde network and their  
727 potential sources, *J. Geophys. Res. Atmos.*, 127, e2022JD037174,  
728 <https://doi.org/10.1029/2022JD037174>, 2022.

729 Zhang, J., J., Guo, S., Zhang, and Shao, J.: Inertia-gravity wave energy and instability  
730 drive turbulence: Evidence from a near-global high-resolution radiosonde  
731 dataset, *Clim. Dyn.*, 58(11), 2927–2939, [https://doi.org/10.1007/s00382-021-](https://doi.org/10.1007/s00382-021-06075-2)  
732 [06075-2](https://doi.org/10.1007/s00382-021-06075-2), 2022.

733  
734  
735  
736  
737  
738  
739  
740  
741  
742

743 **Table 1.** Comparisons of mean wind shears between HVRRS and ERA5 reanalysis at  
 744 heights of 0–2 km a.g.l. (a), 10–15 km a.g.l. (b), and 20–25 km a.g.l. (c).

| <b>(a) Wind shear at 0–2 km a.g.l. (m/s/km)</b>   |       |             |            |         |            |             |       |
|---|-------|-------------|------------|---------|------------|-------------|-------|
|   | Polar | Midlatitude | Subtropics | Tropics | Subtropics | Midlatitude | Polar |
|   | (NH)  | (NH)        | (NH)       |         | (SH)       | (SH)        | (SH)  |
| HVRRS   | 12.60 | 12.72       | 12.10      | 10.64   | 12.82      | 14.12       | 15.35 |
| ERA5  | 8.02  | 9.14        | 8.62       | 5.21    | 8.54       | 10.32       | 8.73  |
| <b>(b) Wind shear at 10–15 km a.g.l. (m/s/km)</b> |       |             |            |         |            |             |       |
| HVRRS   | 13.22 | 14.95       | 13.38      | 9.49    | 13.52      | 14.66       | 13.11 |
| ERA5  | 4.17  | 6.08        | 6.76       | 5.79    | 6.74       | 5.13        | 3.38  |
| <b>(c) Wind shear at 20–25 km a.g.l. (m/s/km)</b> |       |             |            |         |            |             |       |
| HVRRS   | 15.17 | 15.66       | 15.20      | 16.72   | 16.57      | 16.12       | 17.19 |
| ERA5  | 2.85  | 3.48        | 4.03       | 5.22    | 3.92       | 3.33        | 2.90  |

745  
 746  
 747  
 748  
 749  
 750  
 751  
 752  
 753  
 754  
 755  
 756  
 757  
 758  
 759  
 760

761 **Table 2.** The occurrence rate of low  $Ri$  at 0.8–1.3 km a.g.l. (a), 2.2–3.2 km a.g.l. (b),  
762 6–15 km a.g.l. (c), and 20–21 km a.g.l. (d). The critical  $Ri$  ( $Rit$ ) is 1/4 for radiosonde,  
763 and it increases from 1/4 to 2 for ERA5 reanalysis. Note that HVRRS data were  
764 vertically resampled to 100-m, 200-m, 300-m, and 400-m at these four height intervals  
765 to match with the ERA5 reanalysis. In addition, the moving average number in Eq.(1)  
766 is 0. RS stands for radiosonde.

| <b>(a) Frequency of low <math>Ri</math> at 0.8–1.3 km a.g.l. (%) / Vertical resolution of RS is 100-m</b> |       |             |            |         |            |             |       |
|---|-------|-------------|------------|---------|------------|-------------|-------|
|   | Polar | Midlatitude | Subtropics | Tropics | Subtropics | Midlatitude | Polar |
|   | (NH)  | (NH)        | (NH)       |         | (SH)       | (SH)        | (SH)  |
| RS, $Rit=1/4$   | 14.76 | 22.76       | 22.13      | 13.28   | 20.95      | 22.44       | 20.46 |
| ERA5, $Rit=1/4$   | 2.41  | 8.93        | 6.30       | 2.32    | 6.93       | 4.52        | 2.96  |
| ERA5, $Rit=0.5$   | 3.73  | 12.80       | 9.43       | 3.60    | 11.95      | 8.42        | 7.34  |
| ERA5, $Rit=1$   | 8.54  | 21.10       | 22.11      | 8.33    | 26.23      | 19.45       | 15.98 |
| ERA5, $Rit=1.5$   | 13.80 | 29.69       | 31.44      | 12.98   | 36.88      | 28.83       | 24.03 |
| ERA5, $Rit=2$   | 19.04 | 36.78       | 38.50      | 17.08   | 44.21      | 38.03       | 30.18 |
| <b>(b) Frequency of low <math>Ri</math> at 2.2–3.2 km a.g.l. (%) / Vertical resolution of RS is 200-m</b> |       |             |            |         |            |             |       |
| RS, $Rit=1/4$   | 3.00  | 5.60        | 7.40       | 5.48    | 8.87       | 4.29        | 4.12  |
| ERA5, $Rit=1/4$   | 0.22  | 0.60        | 1.00       | 1.33    | 2.29       | 0.28        | 0.11  |
| ERA5, $Rit=0.5$   | 0.37  | 1.03        | 1.96       | 2.10    | 4.23       | 0.50        | 0.18  |
| ERA5, $Rit=1$   | 1.10  | 3.26        | 6.35       | 5.23    | 10.00      | 2.20        | 0.93  |
| ERA5, $Rit=1.5$   | 2.64  | 6.75        | 12.30      | 9.02    | 16.39      | 5.62        | 2.68  |
| ERA5, $Rit=2$   | 4.80  | 10.85       | 18.25      | 13.01   | 22.90      | 9.87        | 5.10  |
| <b>(c) Frequency of low <math>Ri</math> at 6–15 km a.g.l. (%) / Vertical resolution of RS is 300-m</b>    |       |             |            |         |            |             |       |
| RS, $Rit=1/4$   | 0.75  | 2.20        | 3.86       | 6.00    | 4.44       | 1.98        | 0.56  |
| ERA5, $Rit=1/4$   | 0.17  | 0.38        | 0.54       | 1.47    | 0.57       | 0.25        | 0.05  |
| ERA5, $Rit=0.5$   | 0.32  | 1.16        | 1.95       | 4.37    | 2.10       | 0.93        | 0.15  |
| ERA5, $Rit=1$   | 1.38  | 4.33        | 7.73       | 13.14   | 8.90       | 3.52        | 0.61  |
| ERA5, $Rit=1.5$   | 2.93  | 8.32        | 14.54      | 21.79   | 17.05      | 6.76        | 1.38  |
| ERA5, $Rit=2$   | 4.70  | 12.35       | 20.91      | 29.28   | 24.55      | 10.02       | 2.32  |

**(d) Frequency of low  $Ri$  at 20–21 km a.g.l. (%) / Vertical resolution of RS is 400-m**

|                                  |      |      |      |      |      |      |      |
|----------------------------------|------|------|------|------|------|------|------|
| <b>RS, <math>Ri=1/4</math></b>   | 0.03 | 0.07 | 0.12 | 0.04 | 0.04 | 0.10 | 0.07 |
| <b>ERA5, <math>Ri=1/4</math></b> | 0.01 | 0.02 | 0.01 | 0.02 | 0.02 | 0.03 | 0.04 |
| <b>ERA5, <math>Ri=0.5</math></b> | 0.02 | 0.03 | 0.01 | 0.02 | 0.03 | 0.04 | 0.04 |
| <b>ERA5, <math>Ri=1</math></b>   | 0.03 | 0.05 | 0.04 | 0.05 | 0.05 | 0.08 | 0.04 |
| <b>ERA5, <math>Ri=1.5</math></b> | 0.04 | 0.11 | 0.13 | 0.19 | 0.09 | 0.17 | 0.04 |
| <b>ERA5, <math>Ri=2</math></b>   | 0.05 | 0.21 | 0.32 | 0.55 | 0.18 | 0.30 | 0.05 |

767

768

769

770

771

772

773

774

775

776

777

778

779

780

781

782

783

784

785

786

787

788

789 **Table 3.** Vertical wind shears at 0.8–1.3 km a.g.l. (a), 2.2–3.2 km a.g.l. (b), 6–15 km  
790 a.g.l. (c), and 20–21 km a.g.l. (d). Note that HVRRS data was vertically resampled to  
791 100-m, 200-m, 300-m, and 400-m at these four height intervals to match with the ERA5  
792 reanalysis. RS stands for radiosonde.

| <b>(a) Wind shear at 0.8–1.3 km a.g.l. (m/s/km) / Vertical resolution of RS is 100-m</b> |       |             |            |         |            |             |       |
|--|-------|-------------|------------|---------|------------|-------------|-------|
|  | Polar | Midlatitude | Subtropics | Tropics | Subtropics | Midlatitude | Polar |
|  | (NH)  | (NH)        | (NH)       |         | (SH)       | (SH)        | (SH)  |
| RS   | 12.50 | 11.89       | 11.29      | 11.51   | 13.32      | 13.06       | 14.04 |
| ERA5   | 5.50  | 6.14        | 6.67       | 4.92    | 7.09       | 7.00        | 6.23  |
| <b>(b) Wind shear at 2.2–3.2 km a.g.l. (m/s/km)/ Vertical resolution of RS is 200-m</b>  |       |             |            |         |            |             |       |
| RS   | 8.26  | 9.00        | 9.11       | 8.67    | 9.22       | 9.39        | 9.75  |
| ERA5   | 3.70  | 4.50        | 5.25       | 4.67    | 5.44       | 4.73        | 4.20  |
| <b>(c) Wind shear at 6–15 km a.g.l. (m/s/km) / Vertical resolution of RS is 300-m</b>    |       |             |            |         |            |             |       |
| RS   | 8.30  | 9.58        | 9.54       | 7.76    | 9.88       | 9.38        | 8.06  |
| ERA5   | 4.01  | 5.39        | 6.02       | 5.26    | 6.32       | 4.86        | 3.39  |
| <b>(d) Wind shear at 20–21 km a.g.l. (m/s/km) / Vertical resolution of RS is 400-m</b>   |       |             |            |         |            |             |       |
| RS   | 9.07  | 10.37       | 11.55      | 12.50   | 11.99      | 10.48       | 9.94  |
| ERA5   | 2.99  | 3.85        | 4.80       | 5.63    | 4.73       | 3.64        | 2.98  |

793

794

795

796

797

798

799

800

801

802

803

804 **Table 4.** Similar to Tab.1 but for the occurrence frequency of  $Ri < Rit$ . Note that  $Rit$  is  
 805 indicated by  $Ri < 1/4$  in radiosonde, but it is identified with 1 in ERA5 reanalysis.

| <b>(a) <math>OF(Ri &lt; Rit)</math> at 0–2 km a.g.l. (%)</b> |       |             |            |         |            |             |       |
|--|-------|-------------|------------|---------|------------|-------------|-------|
|  | Polar | Midlatitude | Subtropics | Tropics | Subtropics | Midlatitude | Polar |
|  | (NH)  | (NH)        | (NH)       |         | (SH)       | (SH)        | (SH)  |
| HVRRS  | 9.05  | 15.57       | 16.44      | 13.13   | 17.30      | 15.21       | 13.40 |
| ERA5   | 28.02 | 41.26       | 40.36      | 40.14   | 47.45      | 42.92       | 27.59 |

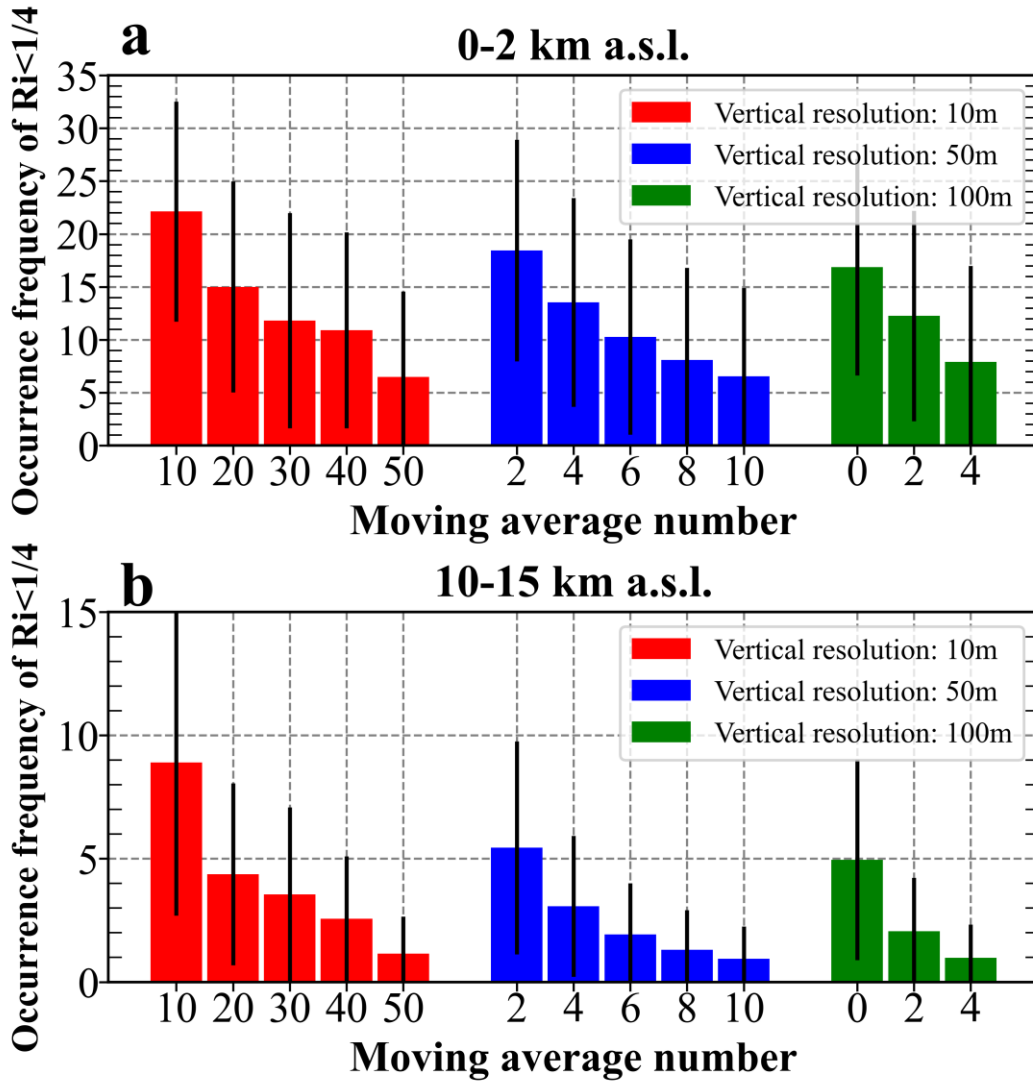
  

| <b>(b) <math>OF(Ri &lt; Rit)</math> at 10–15 km a.g.l. (%)</b> |      |      |      |       |      |      |      |
|--|------|------|------|-------|------|------|------|
| HVRRS  | 0.51 | 2.05 | 5.21 | 11.11 | 6.00 | 1.53 | 0.65 |
| ERA5   | 0.44 | 2.62 | 6.86 | 17.03 | 7.15 | 1.67 | 0.28 |

| <b>(c) <math>OF(Ri &lt; Rit)</math> at 20–25 km a.g.l. (%)</b> |      |      |      |      |      |      |      |
|--|------|------|------|------|------|------|------|
| HVRRS  | 0.45 | 0.48 | 0.42 | 0.51 | 0.38 | 0.67 | 1.53 |
| ERA5   | 0.06 | 0.07 | 0.04 | 0.11 | 0.06 | 0.06 | 0.04 |

806  
 807  
 808  
 809  
 810  
 811  
 812  
 813  
 814  
 815  
 816  
 817  
 818  
 819  
 820  
 821



822

823 **Figure 1.** The averaged occurrence frequencies of  $Ri < 1/4$  at heights of 0–2 km a.s.l. (a)

824 and 10–15 km a.s.l. (b), with vertical resolutions ranging 10-m to 100-m and moving

825 point numbers increasing from 0 to 50. The error bars correspond to the standard

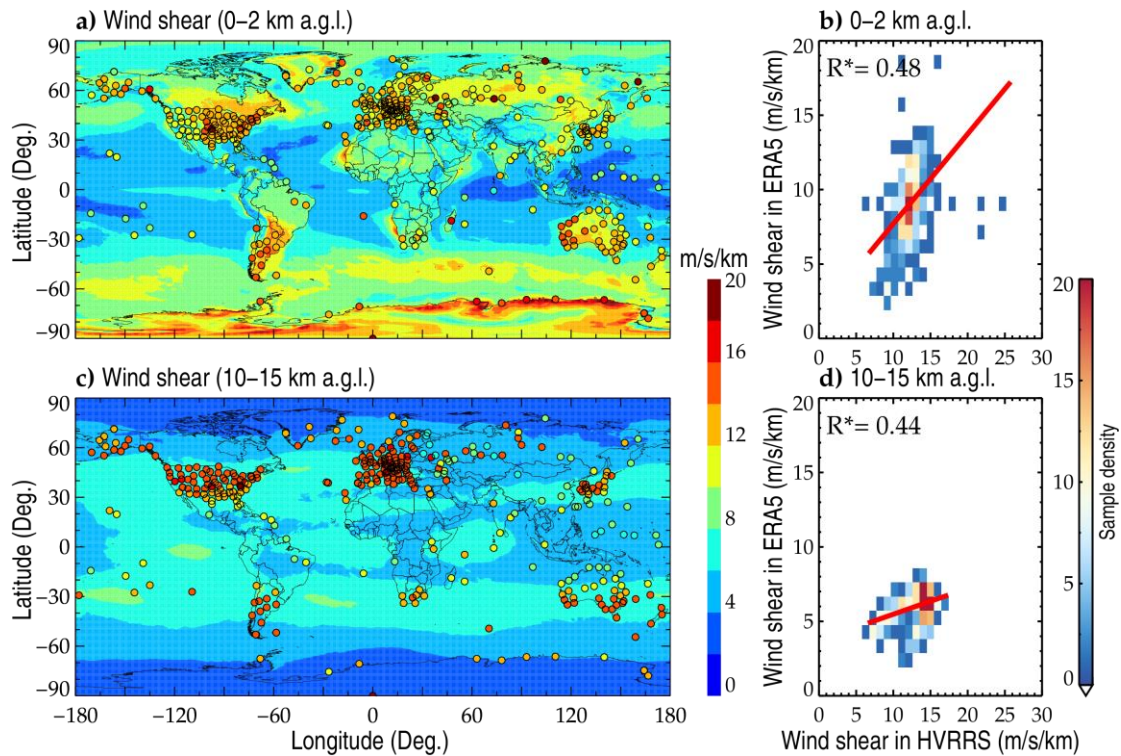
826 deviation. The metrics are counted based on all radiosonde profiles during years 2017–

827 2022.

828

829





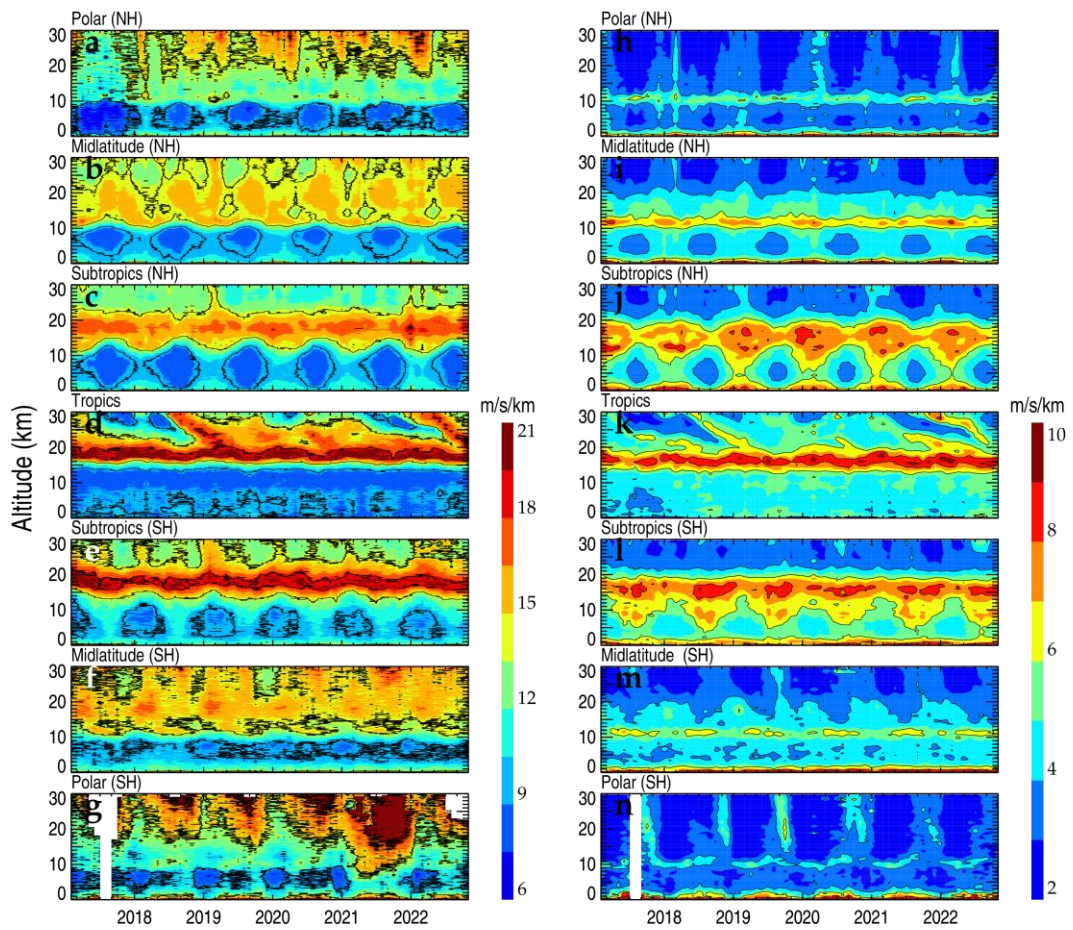
830

831 **Figure 2.** The spatial distribution of mean wind shear in ERA5 reanalysis at heights of  
 832 0–2 km a.g.l. (a) and 10–15 km a.g.l. (c). The overlaid colored circles represent the  
 833 result in HVRRS at the same height levels. Each data point represents a vertically  
 834 averaged value of the wind shear at one radiosonde station during the whole study  
 835 period. Density plots (b, d) show the correlation between wind shears in HVRRS and  
 836 ERA5 reanalysis. The ERA5 derived wind shears are spatially and temporally  
 837 collocated with those of HVRRS. In addition, the red lines represent a least-squared  
 838 linear regression, and the star superscripts indicate that values are statistically  
 839 significant ( $p < 0.05$ ).

840

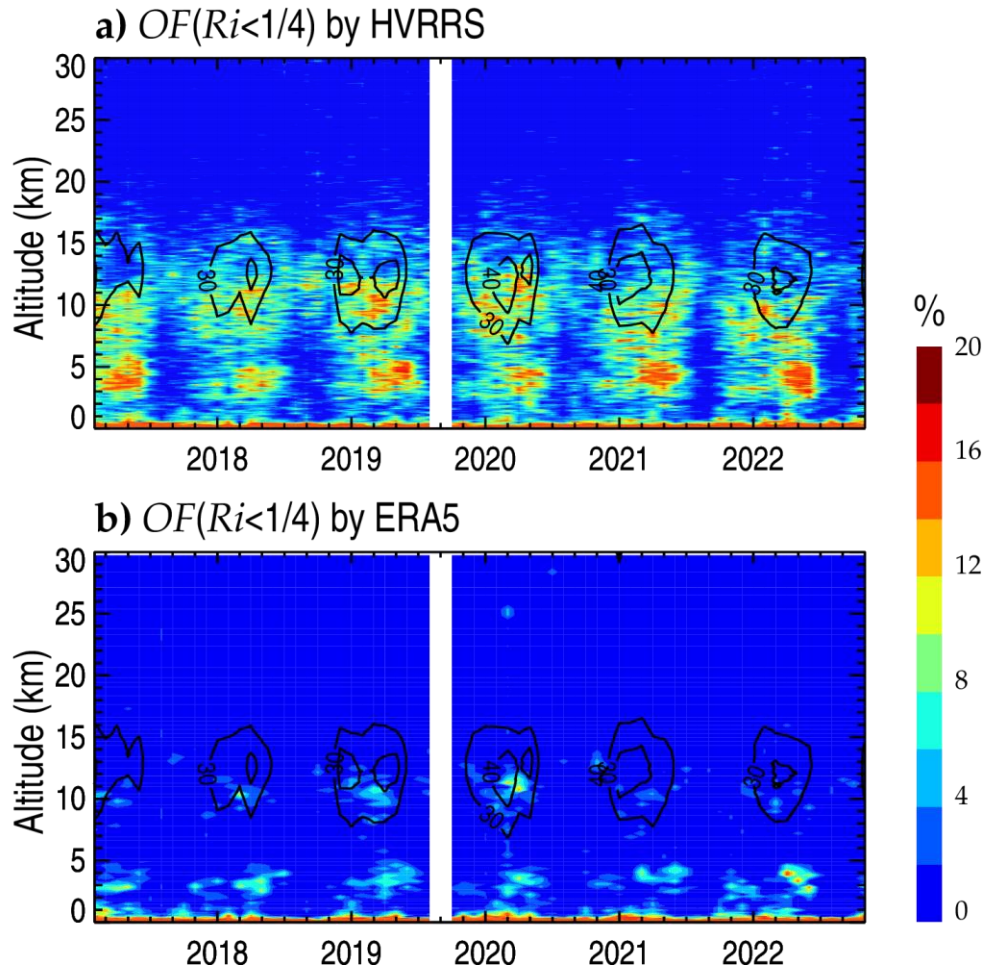
841

842



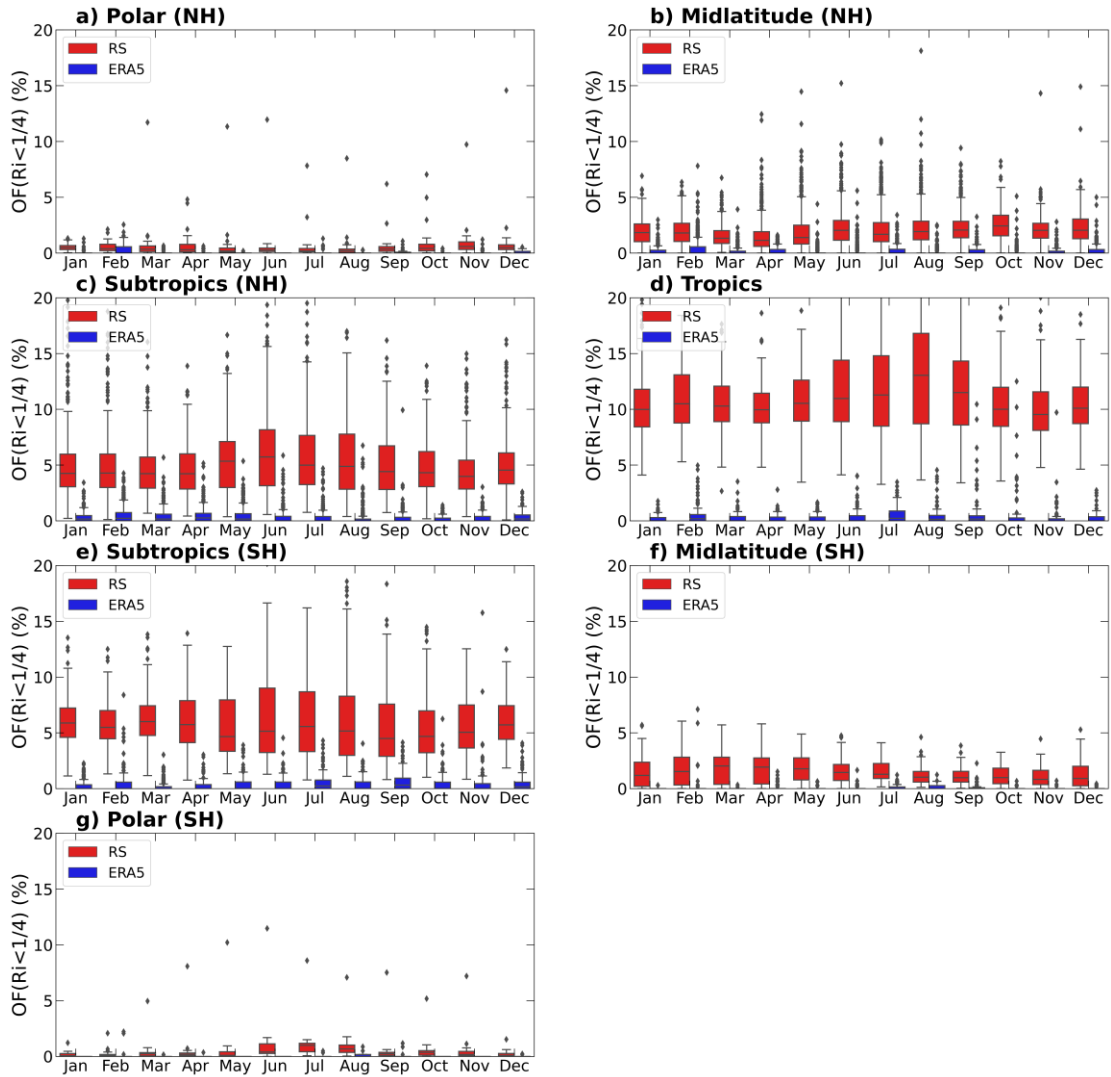
843

844 **Figure 3.** Monthly mean wind shears during years 2017–2022 in HVRRS (a–g) and  
 845 ERA5 reanalysis (h–n) at different climate zones. The ERA5 derived wind shears are  
 846 spatially and temporally collocated with those of HVRRS. NH=Northern Hemisphere;  
 847 SH=Southern Hemisphere.



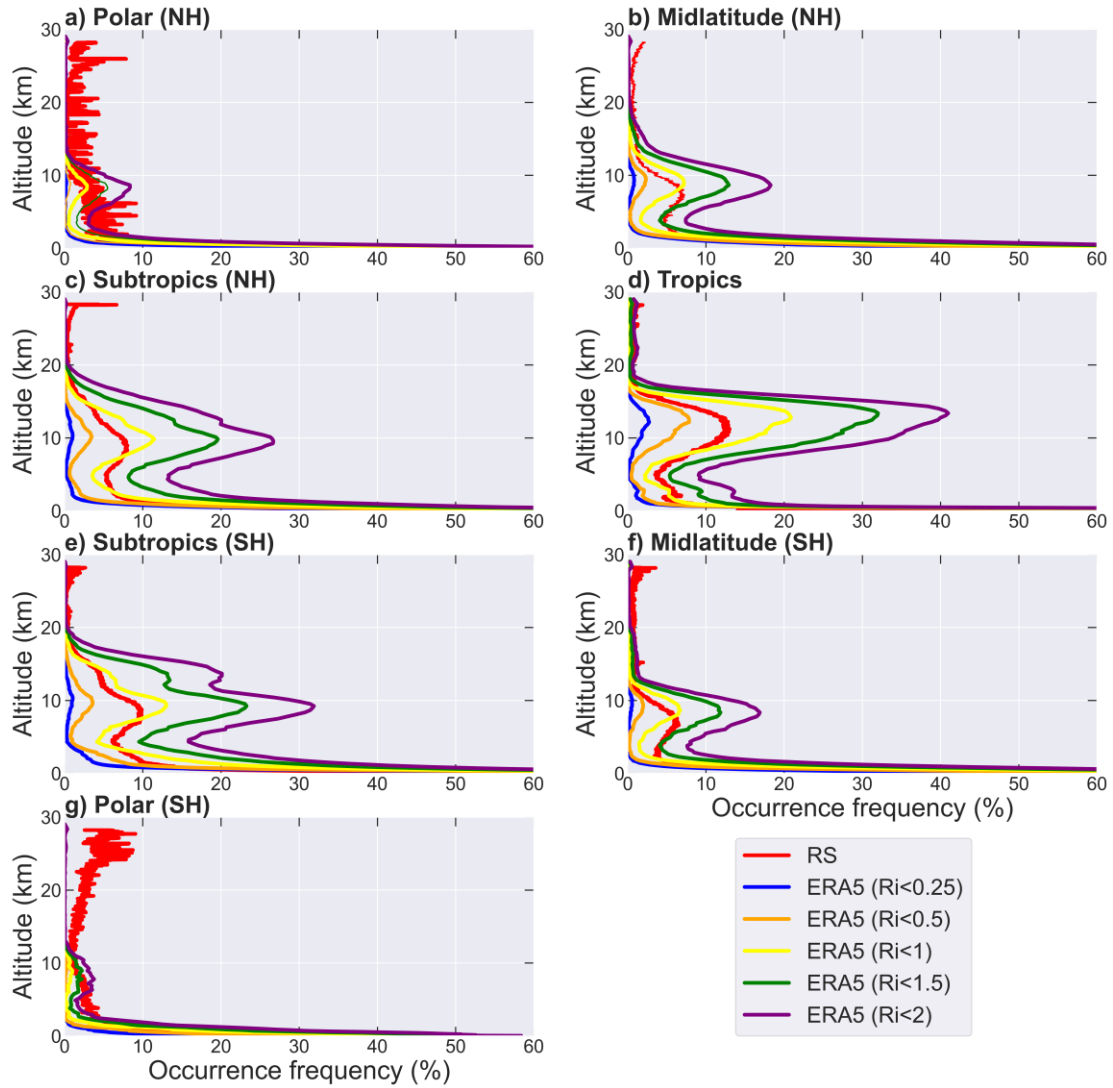
848

849 **Figure 4.** The monthly occurrence frequency of  $Ri < 1/4$  at Corpus Christi station ( $27.77^\circ$   
 850 N,  $-97.5^\circ$ W) in HVRRS (a) and ERA5 reanalysis (b). Note that the contour curves in  
 851 (a) and (b) concern the mean horizontal wind speed, and that the ERA5 derived  
 852 quantities are spatially and temporally collocated with those of HVRRS.



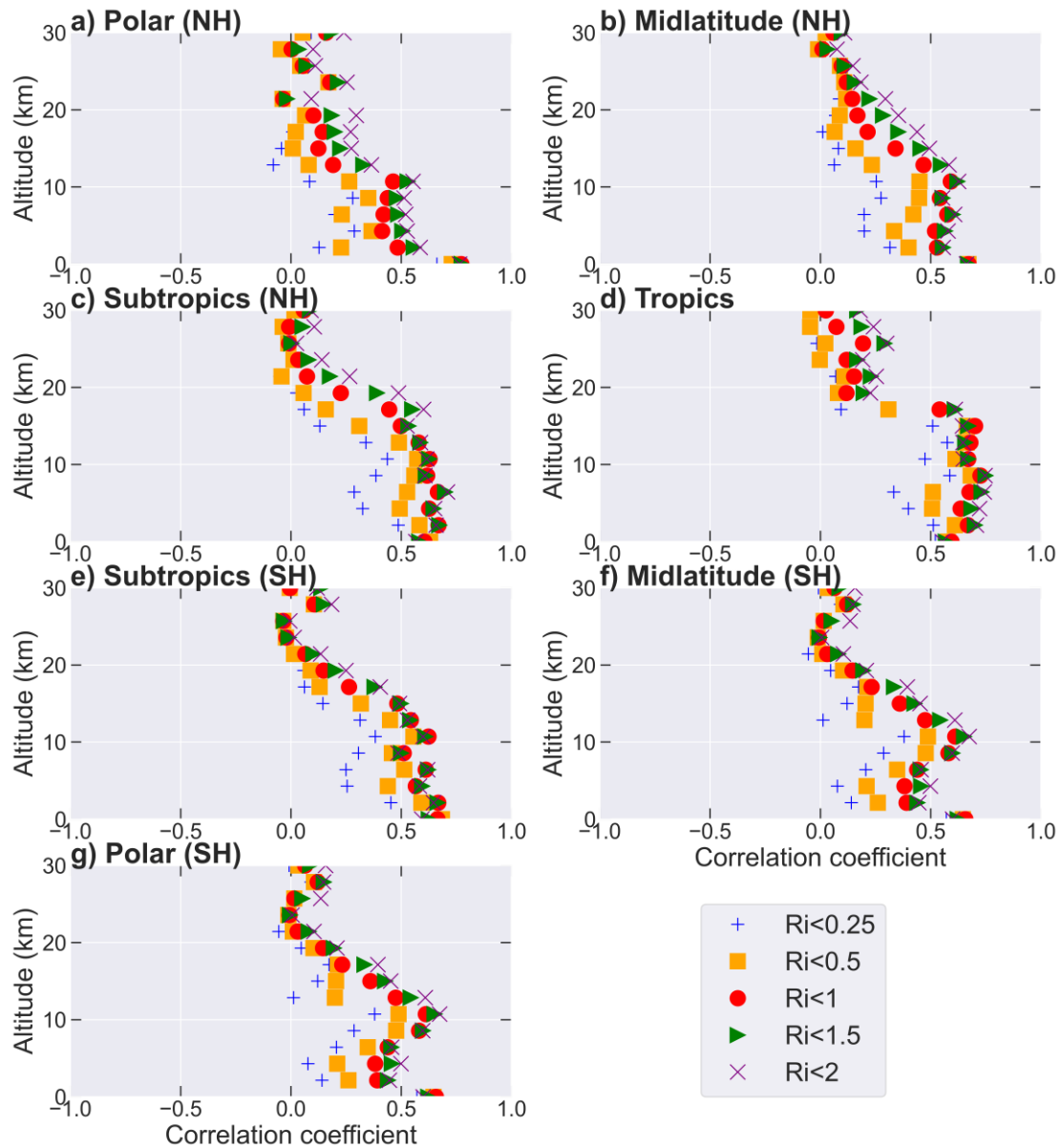
853

854 **Figure 5.** The annual cycles of the occurrence frequency of  $Ri < 1/4$  in different climate  
 855 zones at 10–15 km a.g.l. The red and blue boxes represent the frequencies in HVRRS  
 856 and ERA5 reanalysis, respectively. The ERA5 derived  $Ri$  is spatially and temporally  
 857 collocated with that of HVRRS. NH, Northern Hemisphere; SH, Southern Hemisphere.



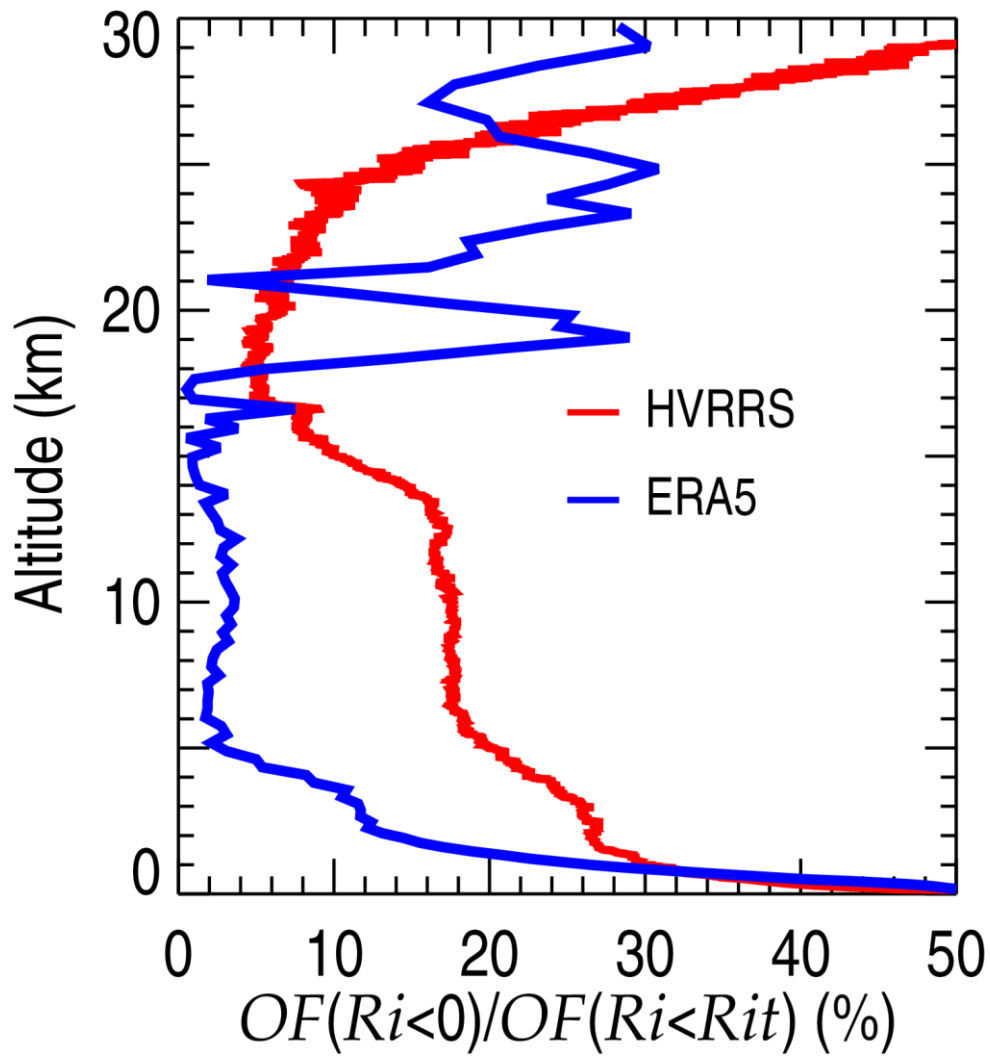
858

859 **Figure 6.** The altitude variation of the occurrence frequency of  $Ri$  below certain  
 860 thresholds (0.25, 0.5, 1, 1.5, and 2) in ERA5 reanalysis in various climate zones. The  
 861 ERA5 derived  $Ri$  is spatially and temporally collocated with that of HVRRS. The  
 862 occurrences of  $Ri < 1/4$  in HVRRS are overlapped with red lines.



863

864 **Figure 7.** The correlation coefficients between monthly averaged occurrence frequency  
 865 of  $Ri < 1/4$  in the HVRRS and the monthly occurrence frequency of  $Ri$  below certain  
 866 thresholds (0.25, 0.5, 1, 1.5, and 2) in ERA5 reanalysis. The ERA5 derived  $Ri$  is  
 867 spatially and temporally collocated with that of HVRRS. The coefficients in various  
 868 climate zones are estimated in an increment of 2 km.



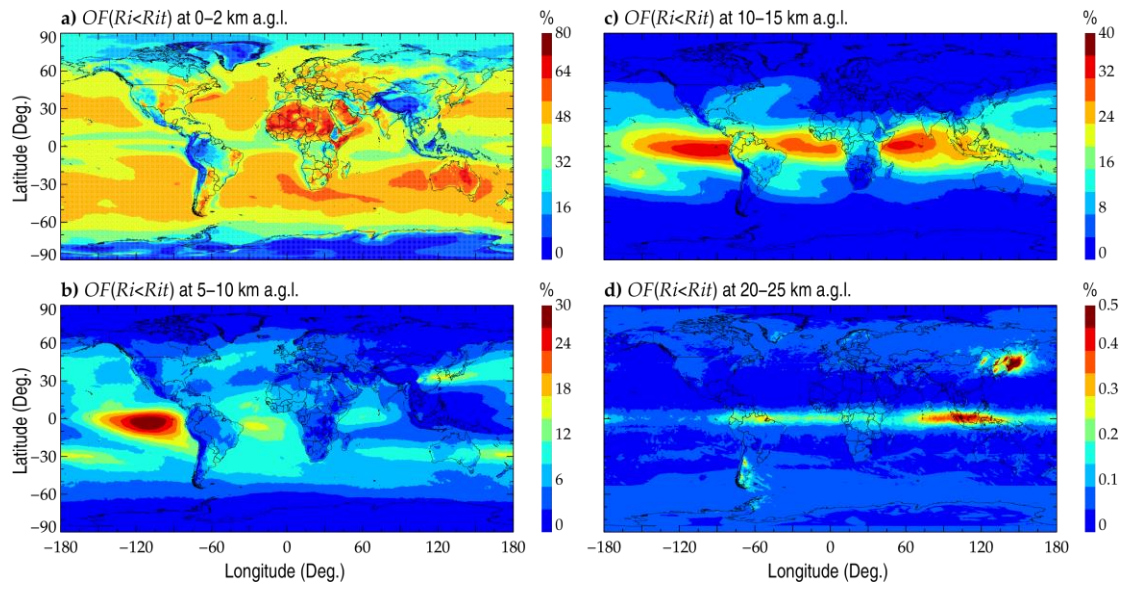
869

870 **Figure 8.** The percentage of  $OF(Ri < 0)$  relative to  $OF(Ri < Rit)$  in HVRRS (red) and  
 871 ERA5 reanalysis (blue).

872

873

874



875

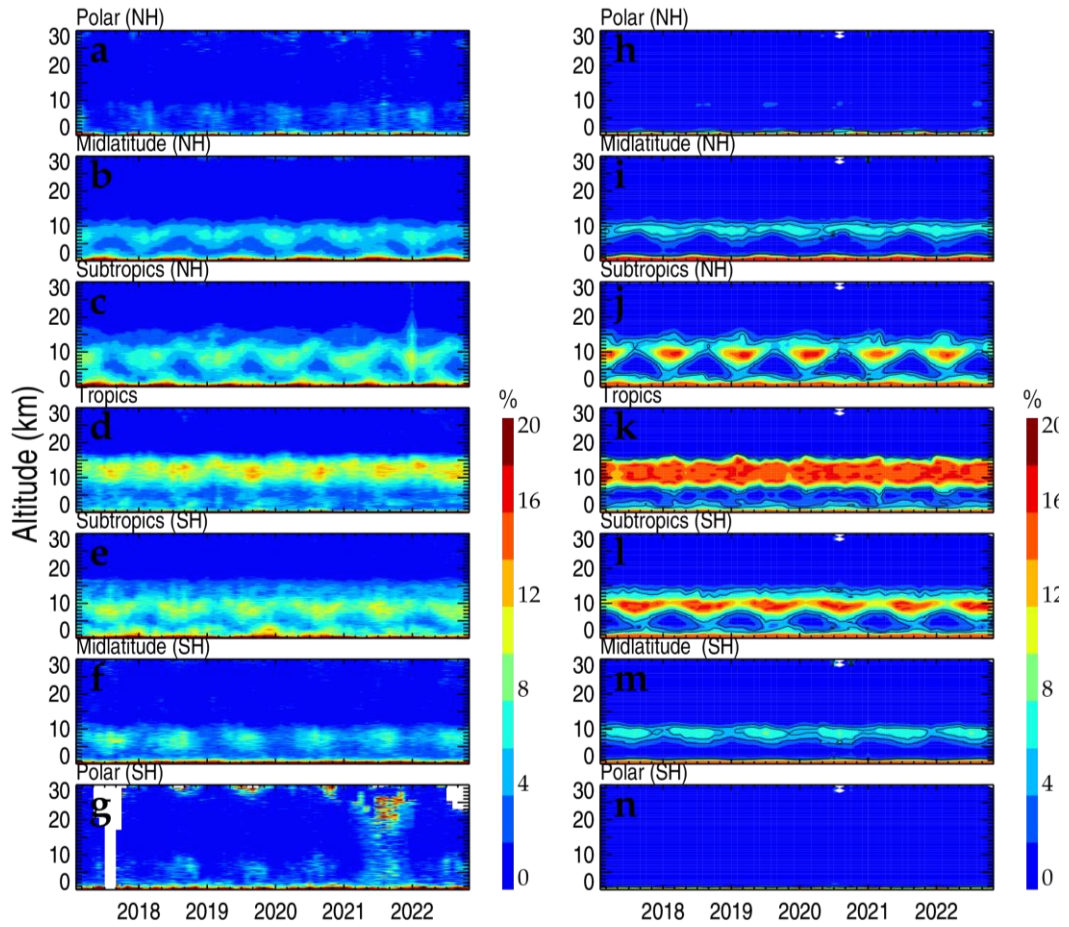
876 **Figure 9.** The spatial distribution of the mean  $OF(Ri < Rit)$  in ERA5 reanalysis at 0–2  
 877 km a.g.l. (a), 5–10 km a.g.l. (b), 10–15 km a.g.l. (c), and 20–25 km a.g.l. (d). Note that  
 878  $Rit$  is set to 1.

879

880

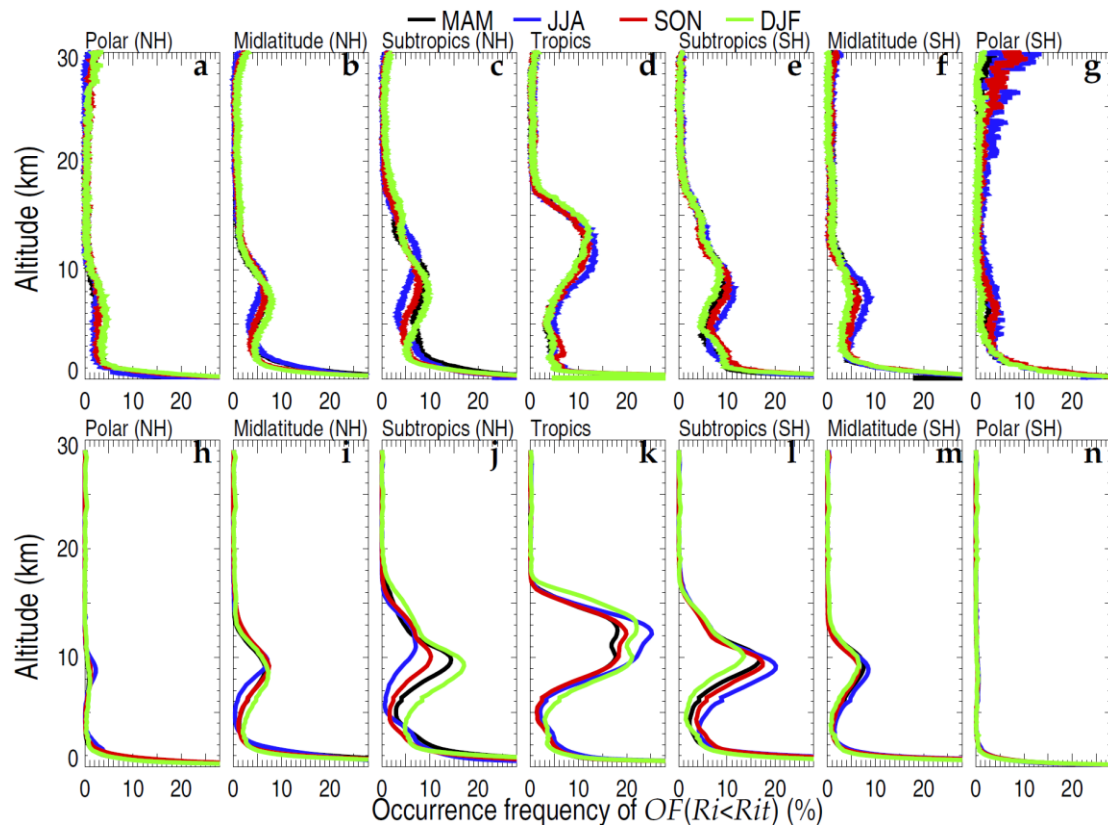
881





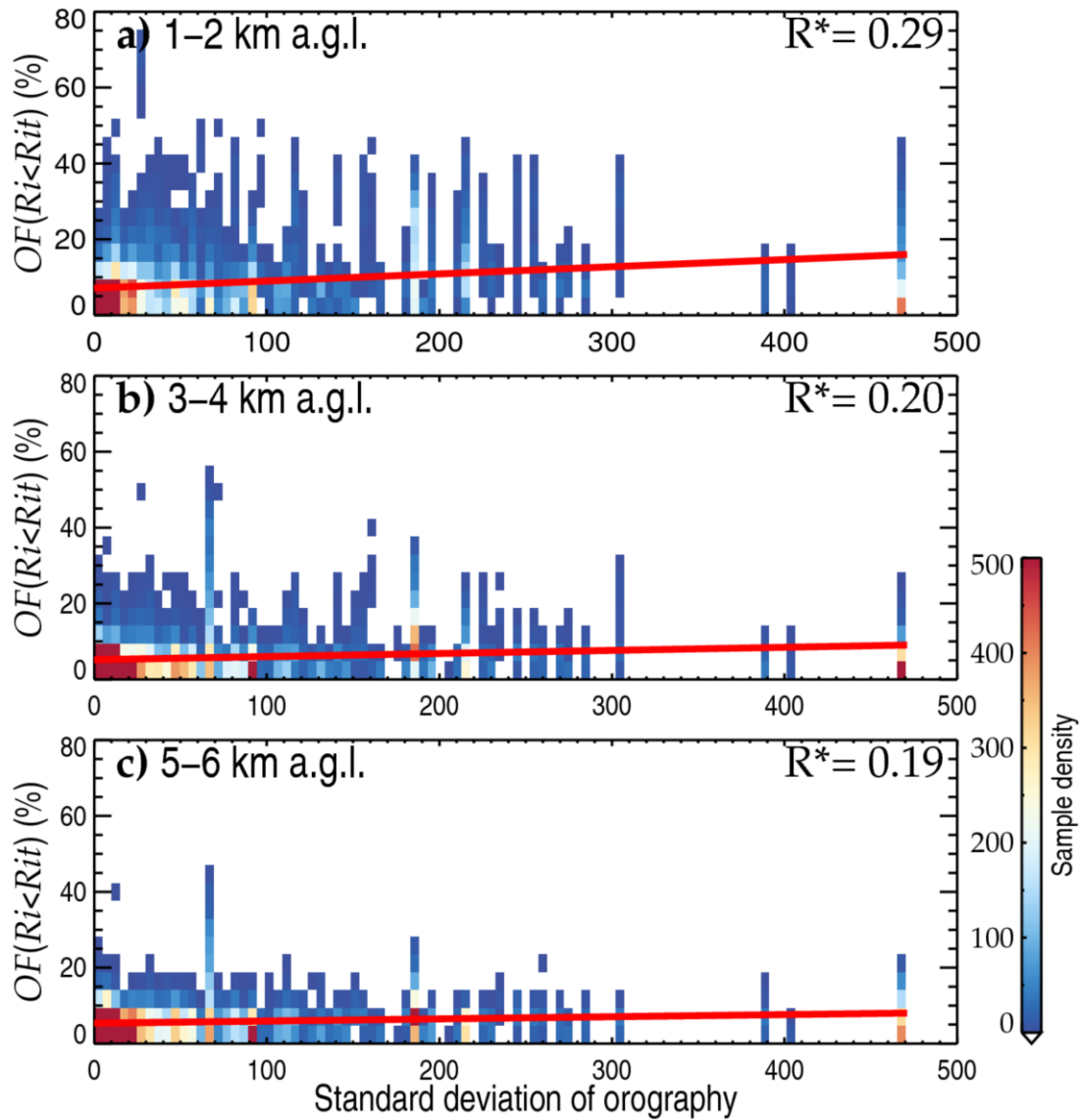
882

883 **Figure 10.** The monthly averaged  $OF(Ri < Rit)$  in the HVRRS (a–g) and ERA5  
 884 reanalysis (h–n) in seven climate zones. NH=Northern Hemisphere; SH=Southern  
 885 Hemisphere.



886

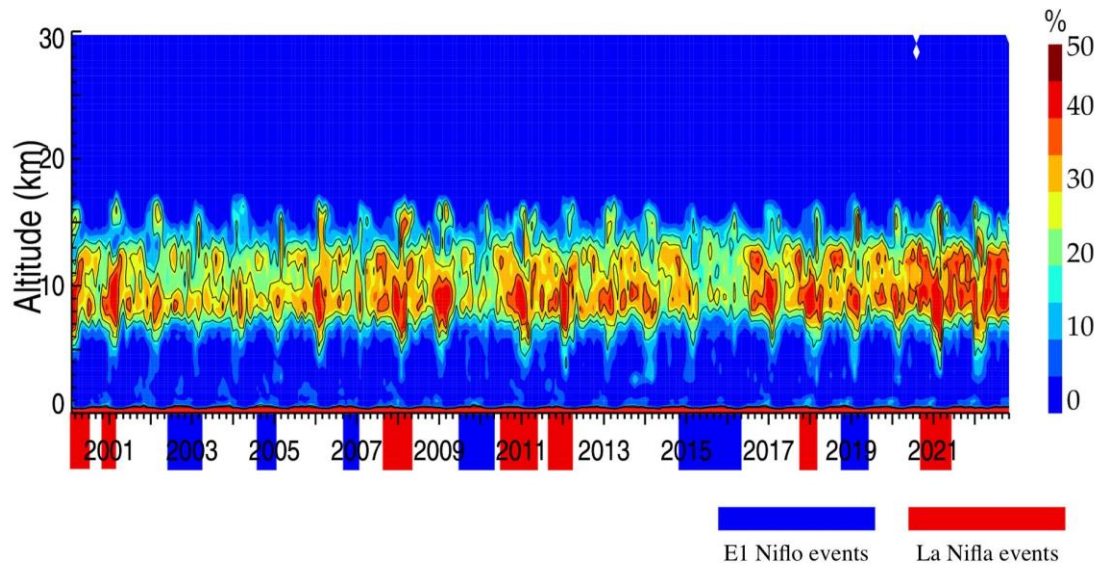
887 **Figure 11.** The seasonal averaged  $OF(Ri < Rit)$  in the HVRRS (a–g) and ERA5  
 888 reanalysis (h–m) in seven climate zones. MAM, March–April–May; JJA, June–July–  
 889 August; SON, September–October–November; DJF, December–January–February.  
 890 NH=Northern Hemisphere; SH=Southern Hemisphere.



891

892 **Figure 12.** The association of HVRRS-determined  $OF(Ri < Rit)$  with different standard  
 893 deviations of orography (dimensionless). (a), (b), and (c) are for height ranges of 1–2  
 894 km, 3–4 km, and 5–6 km a.g.l., respectively. The correlation coefficients between  
 895  $OF(Ri < Rit)$  and standard derivation of orography are marked in the top right corner,  
 896 where the star superscripts indicate that values are statistically significant ( $p < 0.05$ ).

897

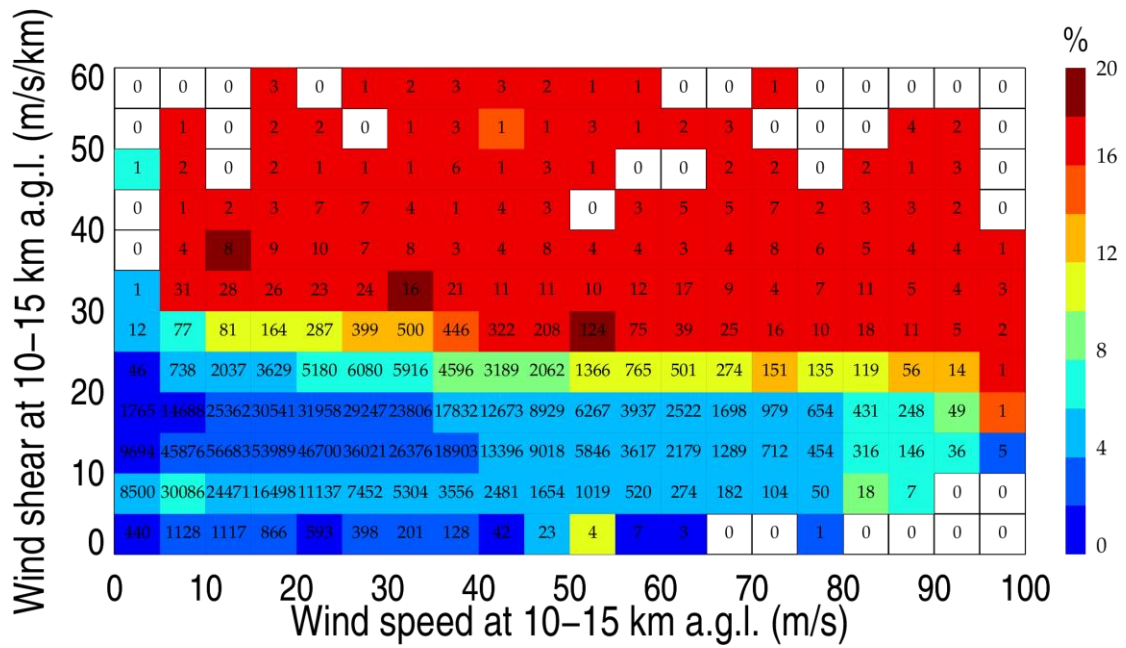


898

899 **Figure 13.** The monthly averaged  $OF(Ri < Rit)$  in ERA5 reanalysis over the Niño 3  
900 region ( $5^{\circ}\text{N}$ – $5^{\circ}\text{S}$ ,  $150^{\circ}\text{W}$ – $90^{\circ}\text{W}$ ). The blue and red shadings in time axis indicate the  
901 time periods with El Niño and La Niña events, respectively.



910



911

912 **Figure 15.** Joint distribution of HVRRS-derived wind speed, wind shear, and  
 913  $OF(Ri < Rit)$ , with a bin size of 5 m/s along the x axis and 5 m/s/km along the y axis.  
 914 Note that all the relationship is based on the mean result of individual profiles at heights  
 915 of 10–15 km a.g.l.. The number indicates the matched profile number in each grid.